geosciences

MDPI

Article

An Attempt to Study Natural H_2 Resources across an Oceanic Ridge Penetrating a Continent: The Asal–Ghoubbet Rift (Republic of Djibouti)

Gabriel Pasquet [1], Rokiya Houssein Hassan [2], Olivier Sissmann [3], Jacques Varet [4] and Isabelle Moretti [1,*]

[1] Laboratoire des Fluides Complexes et leurs Réservoirs (LFCR), E2S UPPA, Université de Pau et des Pays de l'Adour, 64012 Pau, France; gabriel.pasquet@univ-pau.fr
[2] Djiboutian Office for Development of Geothermal Energy (ODDEG), Djibouti 999057, Djibouti; rokiyahoussein0@gmail.com
[3] IFP Energies Nouvelles (IFPEN), 1 et 4, Avenue de Bois-Préau, CEDEX, 92852 Rueil-Malmaison, France; olivier.sissmann@ifpen.fr
[4] SARL Géo2D, 45100 Orléans, France; jacques.varet@gmail.com
* Correspondence: isabelle.moretti@univ-pau.fr

Abstract: Dihydrogen (H_2) is generated by fluid–rock interactions along mid-ocean ridges (MORs) and was not, until recently, considered as a resource. However, in the context of worldwide efforts to decarbonize the energy mix, clean hydrogen is now highly sought after, and the production of natural H_2 is considered to be a powerful alternative to electrolysis. The Afar Rift System has many geological features in common with MORs and offers potential in terms of natural H_2 resources. Here, we present data acquired during initial exploration in this region. H_2 contents in soil and within fumaroles were measured along a 200 km section across the Asal–Ghoubbet rift and the various intervening grabens, extending from Obock to Lake Abhe. These newly acquired data have been synthesized with existing data, including those from the geothermal prospect area of the Asal–Ghoubbet rift zone. Our results demonstrate that basalt alteration with oxidation of iron-rich facies and simultaneous reduction in water is the likely the source of the hydrogen, although H_2S reduction cannot be ruled out. However, H_2 volumes at the surface within fumaroles were found to be low, reaching only a few percent. These values are considerably lower than those found in MORs. This discrepancy may be attributed to bias introduced by surface sampling; for example, microorganisms may be preferentially consuming H_2 near the surface in this environment. However, the low H_2 generation rates found in the study area could also be due to a lack of reactants, such as fayalite (i.e., owing to the presence of low-olivine basalts with predominantly magnesian olivines), or to the limited volume and slow circulation of water. In future, access to additional subsurface data acquired through the ongoing geothermal drilling campaign will bring new insight to help answer these questions.

Keywords: natural hydrogen; Djibouti; geothermy; Asal–Ghoubbet rift; olivine

Citation: Pasquet, G.; Houssein Hassan, R.; Sissmann, O.; Varet, J.; Moretti, I. An Attempt to Study Natural H_2 Resources across an Oceanic Ridge Penetrating a Continent: The Asal–Ghoubbet Rift (Republic of Djibouti). *Geosciences* **2022**, *12*, 16. https://doi.org/10.3390/geosciences12010016

Academic Editors: Giovanni Vespasiano, Massimiliano Vardè, Carmine Apollaro and Jesus Martinez-Frias

Received: 3 December 2021
Accepted: 27 December 2021
Published: 29 December 2021

1. Introduction

Molecular hydrogen or dihydrogen (H_2, hereafter referred to as hydrogen) is a powerful energy source and offers potential as a green alternative to fossil fuels in the near future. However, at present, hydrogen is produced industrially from hydrocarbons by vapocracking, a process that emits CO_2. Alternatives exist, but all consume energy: the use of a methane plasma torch, the electrolysis of water using green electricity, and the production of natural hydrogen ([1], and references therein). When manufactured through electrolysis, hydrogen can also be used as an energy vector to store electricity. However, exploiting natural H_2 that is produced daily in the subsurface is potentially greener and more economical than manufacturing hydrogen [2,3]. Production of natural H_2 first started

in Mali in 2014 [4] and exploration is now active in several other countries. Mid-ocean ridges (MORs) are known to be productive zones for H_2; however, as they are mostly submarine, their exploitation is far from economical. Spreading systems are found on land in two areas worldwide: Iceland and Afar. This study represents a first attempt at the evaluation of natural hydrogen resources in eastern Afar, at the western extremity of the Aden Ridge, including the Gulf of Tadjoura, the Asal Rift, and other active graben structures in the Republic of Djibouti.

The geological contexts suitable for H_2 generation in the subsurface are becoming well known [5,6]. Emanations of H_2 have been described in several settings: ophiolitic massifs, including Oman, New Caledonia, and the Philippines [7,8]; intracratonic basins, which are usually Archean or Proterozoic, including Russia [9], the USA [10], Brazil [11,12], and Australia [13,14]; and MORs [15–18]. Our study area falls within this last category, *sensu lato*, because the Asal Rift corresponds to an early stage of oceanic accretion. Here, we focus on H_2 generation in this context.

1.1. H_2 in MOR Settings

High H_2 concentrations have previously been measured in the hydrothermal vents of oceanic ridges [15,16,18], emanating from both black and white smokers [19] (Figure 1). The fluids in black smokers are high-temperature [20–22] and acidic [23]. Conversely, white smokers, such as the Lost City hydrothermal vent system on the Mid-Atlantic Ridge (MAR), are alkaline (pH ~9–9.8) and relatively low-temperature (40–70 °C; [18]). In both cases, hydrogen is believed to be generated during the serpentinization of ultrabasic rocks, which implies hydration of mantle-derived material [17,24–26]. The hydration reaction involves the oxidation of ferromagnesian minerals, such as olivine or pyroxene, and the associated reduction in water. Although the kinetics of this reaction have been shown to be optimum at 250–300 °C [27], the reaction can occur at lower temperatures. Oxygen isotopes and the presence of lizardite (stable at 118 °C) have been used to confirm the continuum of serpentinization from high (i.e., upper limit at 500 °C) to low (i.e., a few tens of degrees) temperatures [28].

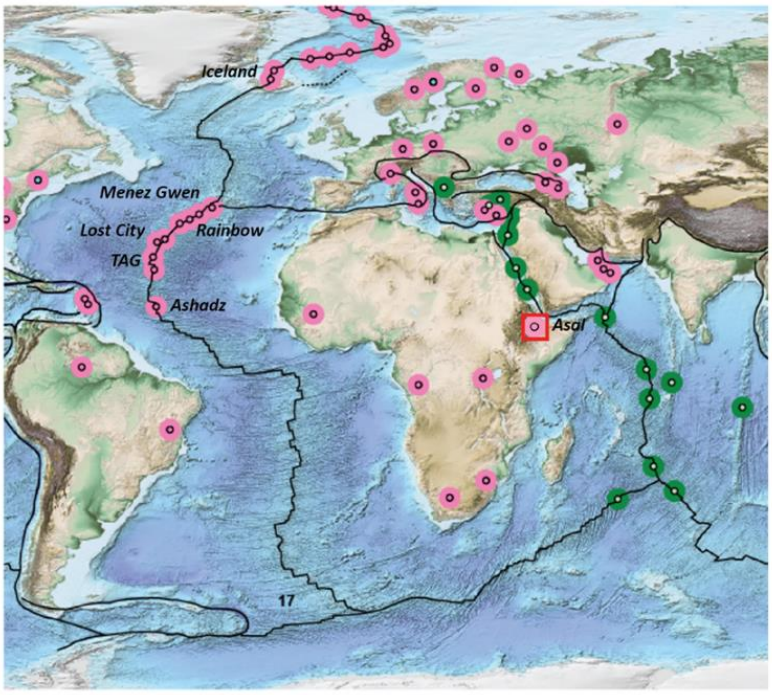

Figure 1. Map centered on the Atlantic Ocean, showing natural H_2 emissions (pink dots) and abiotic CH_4 emissions derived from H_2 (green dots). Locations of some smokers and of the study area (red square) are also shown. (Basemap modified from [2]).

At high temperatures, H_2 may react with CO_2 (via Fischer–Tropsch-type, or FTT, reactions) to produce reduced carbon species, such as abiotic methane (see the green dots of the Red Sea area in Figure 1).

At MORs, sea water interacts with peridotites during serpentinization. Fluid gets infiltrated downward through faults and fracture networks. At fast-spreading ridges, the thin crust (i.e., 6–10 km) allows water to reach mantle-derived rocks. Conversely, at slow-spreading centers, water can come into contact with mantle-derived rocks exposed by transform faults and low-angle normal faults [29,30]. Significant differences in H_2 production have been observed between hydrothermal vents located on peridotitic and basaltic bedrock [18,31]. Indeed, hydrogen production is known to be higher in ultrabasic rocks (e.g., the Ashadz and Rainbow hydrothermal fields) than in basic rocks (e.g., TAG, Menez Gwen) [32]. Olivine, especially its Fe-rich endmember fayalite, is the mineral most likely to generate H_2. Its dissolution kinetics are faster than those of most silicates [33,34]; accordingly, its oxidation is faster and it generates more H_2 during alteration than pyroxenes [35]. Thus, olivine-rich peridotites can potentially produce more H_2 than pyroxene-rich peridotites via alteration to serpentine, magnetite, and brucite [36,37]. Basalts, which are poor in olivine and rich in Al and Mg, tend to form chlorite and smectite clay minerals [38–40]. These argillization reactions produce less Fe^{2+} from the ferrous minerals (oxidized to Fe^{3+}; [41] relative to serpentinization and, therefore, reduce less water to form H_2. However, other reactions (e.g., from H_2S) may result in H_2 generation, as shown in Figure 2.

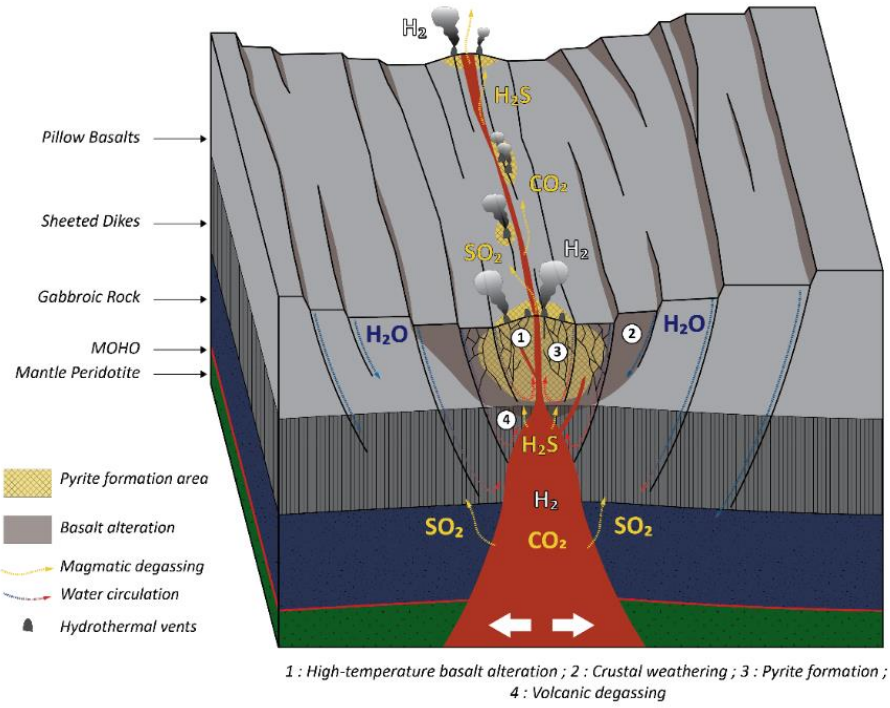

Figure 2. Simplified model of gas production and reaction along an accretionary axis. 1—High-temperature basalt alteration: $3(Fe_2SiO_4)_{rock} + 2H_2O \rightarrow 3SiO_2 + 2Fe_3O_4 + 2H_2$; 2—Crustal weathering: $2Fe_{rock} + H_2O \rightarrow Fe_2O_{3(rock)} + H_2$; 3—Pyrite formation: $FeS + H_2S \rightarrow FeS_2 + H_2$; 4—Volcanic degassing: $SO_2 + 3H_2 \rightarrow H_2S + 2H_2O$. (After [42–44]).

Previously, spreading ridges have been studied primarily to better understand the growth of new oceans, the formation of oceanic crust (layered or otherwise), and the development of life in deep ecosystems [19,20,42,43]. In these contexts, H_2 is a reaction by-product and/or an energy source consumed by microorganisms. When considering hydrogen as a resource, it is important to find areas in which it can be produced both practically and economically. MORs are located offshore and often distant from consumers;

such conditions are likely to preclude economical production. However, some populated areas are located close to areas in which mantle plumes allow these ridges to emerge, as in Iceland. In the Afar Rift System, three extensional zones merge: the southern part of the Red Sea, the northern part of the East African Rift, and the southern part of the Gulf of Aden, which is an active ridge with oceanic crust production occurring onshore [44]. Although MORs are known to emit H_2 (Figure 1), uncertainty remains regarding the existence and volume of such emissions in these two onshore cases. In Iceland, geothermal activity is well developed and H_2 emissions are high in the hot steams along the central axis of the plate boundary [31,45,46]. Geothermal exploration is currently underway, using H_2 geothermometers based on gas–solid reactions at temperatures considered relevant to commercial electricity production (200–350 °C) [47–50]. In the East African Rift System (EARS) and the three branches of the Afar triple junction, the data are more sparse. The present study aims to present new data collected within the Republic of Djibouti, in collaboration with the authority in charge of geothermal development (ODDEG). We also investigate the possibility of joint production of hot water/steam and H_2 in this region.

1.2. Geological Context

1.2.1. Large-Scale/Geodynamic Context

The EARS extends more than 4000 km, from the Red Sea and the Gulf of Aden in the north to Mozambique in the south. It separates the Nubian Plate to the west from the Somali Plate to the east and the Arabian Plate to the north [51,52]. While the Red Sea and the Aden Ridges, including their Afar connection, are of oceanic type, further south, the EARS is composed of numerous interconnected continental rift segments [53]. Broadly, this system can be divided into two main branches. The almost amagmatic western branch extends north–south for approximately 2100 km, from south of Ethiopia to Mozambique. The magmatic eastern branch runs for approximately 2200 km from southern Afar in the north to the Tanzanian rift in the south [54,55]. The Asal Rift, the subject of this study, is located at the western end of the Gulf of Aden and on the northeastern edge of the Afar Depression.

From 31 Ma, an important mantle plume developed below Ethiopia, Kenya, the Republic of Djibouti, Eritrea, and Yemen [56,57]. This plume resulted in a series of basaltic eruptions evolving to siliceous traps during later episodes, producing a total eruptive volume of ~350,000 km^3 [58] and forming the present-day Ethiopian and Yemen highlands. It also marked the beginning of rifting in the Gulf of Aden [57]. Subsidence and active continental rifting in the Red Sea, the Gulf of Aden, Afar, and the Ethiopian Rift started at 25 Ma [51]. The oceanic–continental transition crust has been dated to 20–17 Ma in the Gulf of Aden [44,59]. Subsequently, during the Miocene, tectono-magmatic activity intensified and crustal thinning became active in the different rift branches [51], while oceanic accretion started in the Gulf of Aden. Extension and volcanism continued during the Pliocene, with the formation of the Central Main Ethiopian Rift (CMER) at 8 Ma; this formed the junction between the southern and northern branches of the Ethiopian Rift [57]. After a quiescent phase between 15 and 5 Ma, the Red Sea opening reactivated [60]. The tip of the spreading center of the Gulf of Aden was, during this period, at a similar longitude to the easternmost coast of Djibouti. From the Plio–Pleistocene onward (i.e., 4 Ma–Present), oceanic crust formed in the southern Red Sea, the Afar region, and the Gulf of Tadjoura [51], first as fissural basaltic piles (known as stratoid series) and then from well-defined spreading segments known as axial ranges. These different spreading segments have been connected by transform fault zones over the last million years, forming the axial volcanic ranges of Afar according to an en échelon arrangement [61–64]. These segments comprise a series of active volcano-tectonic ranges, from the Erta Ale range in the north to the Asal range in the southeast [65,66]. The Manda–Hararo–Tendaho–Goba'ad segment links the Red Sea and Aden systems [66,67] and is where the Main Ethiopian Rift (MER) ends. In the MER, which has remained continental, crustal thinning and volcanic activity continue, with a spreading rate much lower than that in Afar (5–7 mm/a versus 2 cm/a; [68,69]. This activity is marked

by the formation of a fault belt, comprising dextral en échelon segments in the Ethiopian Rift that accommodate NW–SE oblique extension [70]. Thus, the Afar depression can be divided into three large units: the Red Sea and the Gulf of Aden megastructures (which trend NNW–SSE and WNW–ESE, and are typically of oceanic ridge type), and the northern end of the continental MER (which trends NNE–SSW) [61,71].

1.2.2. The Asal/Ghoubbet Area

Four grabens oriented in the N130° direction [72] are present in the southern part of the Republic of Djibouti (Figure 3); from north to south, these are the Asal–Ghoubbet, Gaggade, Hanle, and Goba'ad (Lake Abhe) grabens. These grabens exhibit approximately the same trend as the Red Sea and Gulf of Aden spreading segments. The Asal–Ghoubbet graben is connected to the Gulf of Aden ridge via a transform fault [62,73] and exhibits some unusual characteristics in terms of magmatic activity, opening velocity, and heat flow [74–76]. In terms of geography, the Ghoubbet graben is a bay located at the western extremity of the Gulf of Tadjoura, to which it is connected by two narrow passes that are 200 and 450 m wide. The emerging part between the open sea and Lake Asal is approximately 7 km long, and the lake itself currently lies 154 m below sea level. The lake is bordered, particularly at its western tip, by a salt canopy. Salinity in the lake is high at ~350 g/L, which is 10 times higher than the salinity of the open ocean [77,78]. The current climate is very dry; accordingly, the water in the lake is sourced primarily from the sea through faults and fracture networks [64,79,80]. The high seismicity of the area is evidence of its tectonic activity [74].

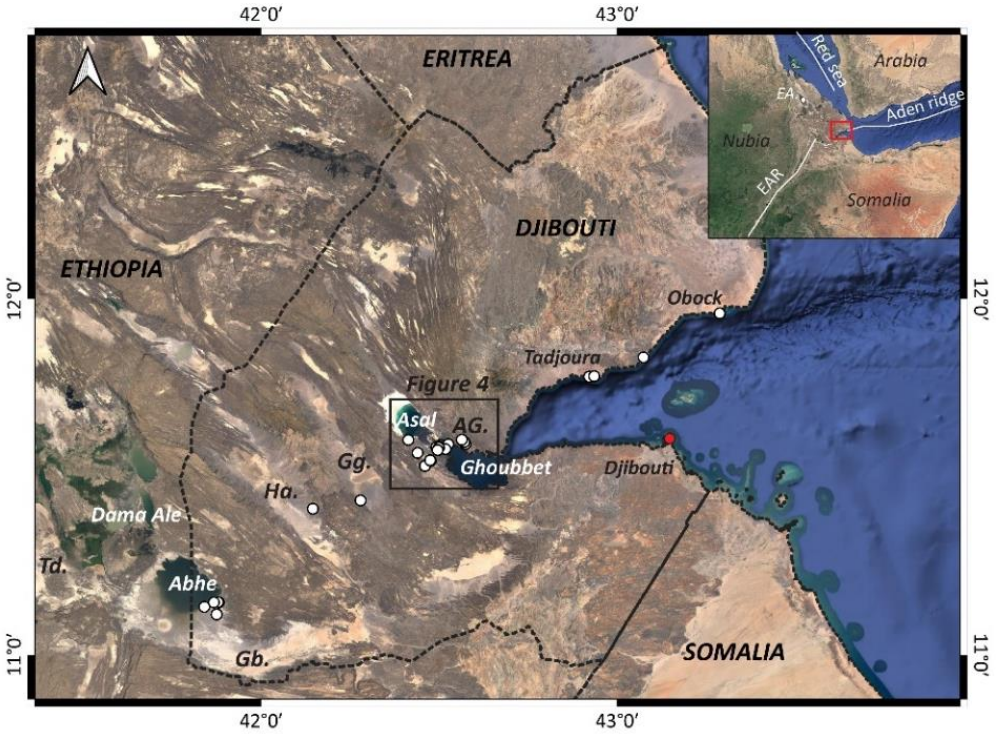

Figure 3. Satellite map illustrating the 3 main axes of the Afar Depression and a close-up on the Djibouti side showing sampling sites and major structures. EAR: East African Rift; AG: Asal–Ghoubbet graben; Gg: Gaggade graben; Ha: Hanle graben; Gb: Goba'ad graben; Td: Tendaho; EA: Erta Ale.

The rate of opening during the Pleistocene (<1.5 Ma) was approximately 1.5 to 2 cm/a in the N40° direction [81,82]. The Asal–Ghoubbet rift zone crosscuts a basaltic series with alkaline tendency of Mio–Pliocene age (4–1 Ma), the Stratoïd Series [66,83]. The rift zone exhibits a vertical topographic gradient along its axis, with maximum elevation differences

of 300 m between Lake Asal and the Fiale Caldera and 150 m between the latter and the Ghoubbet graben. The vertical displacement rate of the faults here has been estimated to be 1–2 mm/year. The rift axis is formed by a series of transitional basalts with a tholeiitic trend, ranging from magnesian basalts to ferro-basalts. This enrichment is the product of advanced plagioclase fractional crystallization [64]. The Asal–Ghoubbet Rift can be divided into three zones (Figures 3 and 4): the outer margins, the inner margins, and the volcanic axial zone. Evolution of lavas from the outer margins to the axial zone has been observed, from porphyritic lavas on the margins to aphyric lavas in the center [64]. The basalts outcropping in the outer margins are between 325 and 87 ka old. These basalts, which constitute the base of the internal series, are covered by flows with ages between 87 and 66 ka. The more recent axial volcanic series has been dated to between 10 ka and today: the Ardoukoba eruption of 1978 [84,85].

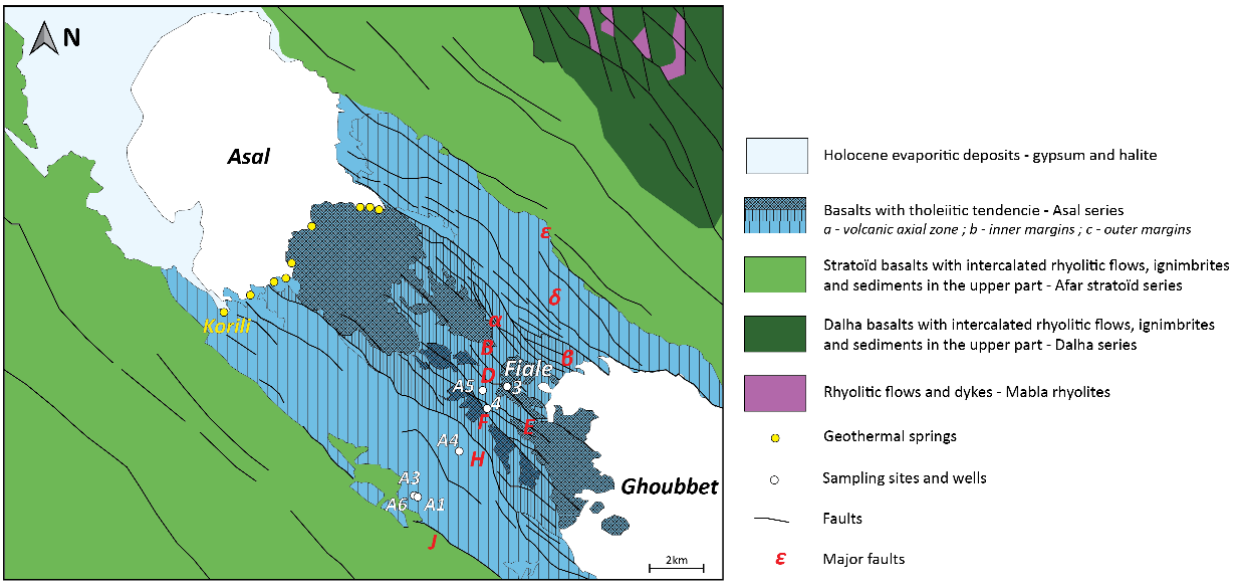

Figure 4. Geological and structural map of the Asal–Ghoubbet Rift. Major fault names are shown in red (Greek alphabet in the northeast and Latin in the southwest), Asal hot springs in yellow (modified from [64,66]) and wells in white.

In contrast to the inner margins, which are rich in plagioclase phenocrysts, the outer margins (i.e., the earliest flows) tend to be rich in olivine phenocrysts. These flows in the outer margins are associated with calcic augites and plagioclases and are picritic basalts [63]; the calcic plagioclases present range from labradorite (An > 50) to bytownite (An > 70) [85]. The absence of orthopyroxene and the presence of calcic augite and stable olivine in the mesostasis of the outer margins should also be noted. In contrast, the axial zone is formed by fissure lavas that are also rich in plagioclases, with an aphyric texture characterizing the later flows, which are richer in iron (FeO > 15%) than the earlier flows. They are formed of andesine, ferriferous augite, and olivine at 60% fayalite. The most abundant basalt in this rift is an andesine basalt, which is found in both the margin zones and the axial zone. In the latter, the plagioclase is andesine and the olivine is approximately $Fa_{30–40}$ [64].

1.2.3. Available Subsurface Data

Within the rift, the major faults exhibit relatively high dips, ranging from 50° to 70° for external faults and up to 80° for more recent internal faults. Seismic surveys have revealed a seismogenic zone centered under the Fiale Caldera (see [74], and references therein). This caldera is located in the axial zone between major faults D and B, which exhibit a NW–SE trend, and is a phreato-magmatic crater with a diameter of 1.3 km. The caldera hosted a lava lake, which overflowed its southern rim toward the Ghoubbet graben. Earthquakes

here typically occur at depths of 2–4 km. More proximal earthquakes, at depths of 0–1 km, occur between the α and δ faults along the NE margins [74] (see Figure 4). In addition, maps and sections of P-wave velocity anomalies show negative anomalies centered on the Fiale Caldera at the surface and at 5 km depth. The caldera is surrounded by a positive seismic velocity anomaly interpreted as a high-temperature zone (600–1200 °C) between 2 and 5 km depth. This anomaly is 2 km wide and the aseismic zone below (i.e., extending from 5 km depth) is considered to be the active magma chamber. Close to the surface, at depths of 0–1.5 km, marine intrusions have been identified with regular flow from Ghoubbet Bay to the lake, channeled primarily through the "petit rift" north of the magmatic axis. Additional water inflow occurs in the first 500 m between major faults F and D, slightly southwest of the Fiale Caldera [74], as confirmed by geothermal wells drilled in the rift.

Geothermal wells A1, A2, A3, A6, and A4 are located on the southwestern outer margin of the rift, and were drilled in the 1970s and 1980s. These wells exhibited a variable but high geothermal gradient between 150 and 300 °C/km. Well A5 is located on the southwestern edge of the Fiale Caldera, in the inner margin; unlike the other wells, this well exhibited a temperature inversion between 400 m and 800 m depth, where the temperature dropped from 175 °C to 65 °C. The velocity anomalies indicate that this inversion is related to a marine intrusion, focused between major faults H and B, which produced cold, fast fluid transfer through faults and fractures from Ghoubbet Bay to Lake Asal, which is 156 m deeper. The temperature was found to increase steadily beyond 800 m depth. For the deepest wells, A5 and A4, bottom-hole temperatures were found to exceed 340 °C [86,87]. On the southern rift margin, which lies outside the cold fluid pathways within the axial corridor, fluid circulation is considered to be slow and the fluids to be warm [79]. These fluids are of chlorine–sodium type, with compositions similar to that of the seawater in the A4 well. The geothermal fluids from the deep reservoir on the margin are hypersaline, with pH ~5 in all cases [88].

1.2.4. Available Gas Analysis Data

Gas composition data are available for wells A3 and A6 (Table 1). The dry gas phase in these boreholes is dominated by CO_2, and the H_2 and H_2S contents are relatively low. The isotope signatures of $\delta^{13}C$ for CO_2 and CH_4 suggest mixing between mantle-derived carbon and carbon of sedimentary origin [88]. The influence of the upper crust is greatest at the external margins of the rift, whereas the CO_2 is mostly of mantle origin within the rift axis. Isotopic signatures for δ^2H-H_2 are available only for well A6. A δ^2H-H_2 value of -436 ‰ V-SMOW and a δ^2H-CH_4 SMOW value of -169 ‰ were measured; these values correspond to equilibrium temperatures of approximately 270 °C and 292 °C according to the equations of [89,90], respectively. Using the data from this previous study, calculating equilibrium temperatures using Bottinga's (1969) equation for $\delta^{13}CH_4$ and CO_2 yielded temperatures of approximately 281 °C, 309 °C, and 332 °C for wells A5, A6, and A3, respectively; these values correspond well with the δ^2H paleothermometer for well A6. No δ^2H data are available for well A5; the concentration presented in Table 1 was obtained from a fumarole close to the well head.

Table 1. Gas composition and isotopic data from Asal wells and fumaroles. GW: geothermal well; F: fumarole; (1) [88]; (2) [91]; (3) [92].

	A3 (GW) (1)	A3 (GW) (2)	A6 (GW) (1)	A5 (F) (2)	Ardoukoba 1978 (F) (3)	N Ghoubbet (F) (2)
CO_2 (mol%)	97.9	99.1	97.5	9.1	16.925	16.5
H_2S (mol%)	0.23	0.23	0.18	0.003	0.0076	0.061
H_2 (mol%)	0.22	0.25	0.16	0.037	0.145	0.1
SO_2 (mol%)	-	-	-	-	82.525	-
CH_4 (mol%)	0.09	0.16	0.09	0.0009	-	0.023
N_2 (mol%)	1.6	0.29	2	70.8	-	65
O_2 + Ar (mol%)	-	0.04	-	20.1	-	18.4
He (mol%)	0.0014	-	0.0018	-	-	-
CO (mol%)	-	-	0.00012	-	0.365	-
R/R_A	12.3	-	-	-	-	11
$\delta^{13}C$-CO_2 PDB ‰	−3.11	−3	−2.62	−5.7	−5.3	−3.1
$\delta^{13}C$-CH_4 PDB ‰	−17	−25.9	−27	−32.1	-	−17
$\delta^{2}H$-H_2 SMOW ‰	-		−436	-	-	-
$\delta^{2}H$-CH_4 SMOW ‰	-		−169	-	-	-
$\delta^{34}S$-SO_2 CD ‰	-		-	-	−2.775	-

Helium data indicate R/R_A ratios of 12.3 and 11 for well A3 and in the northern part of the Ghoubbet area, respectively [91]. These signatures are typical of a mantle origin and are intermediate between OIB and MORB. At the time of the 1978 eruption of Ardoukoba (a volcano in the axial rift zone), the dry volcanic gas mixture (at 1070 °C) was found to be dominated by SO_2, with values above 80 mol% after correction for air and water vapor (up to 79 ± 3 mol%). The isotopic signatures of $\delta^{34}S$-SO_2 suggest the sulfur is also of mantle origin [92]. Well A5 and the North Ghoubbet fumaroles exhibit high contamination from atmospheric air in their gas contents; this can be attributed to the sharp relief. Faults and fractures are open, and the air circulates easily through.

1.2.5. Available Water Analysis Data

As noted previously, the fluid in the rift zone circulates from SE to NW, from the Ghoubbet Sea to Lake Asal, where it evaporates. As a result, numerous hot springs are present along the southeastern rim of Lake Asal. Asal springs are derived from shallow water circulation inside the rift. The springs fed by the marine water intrusion that occurs along the faults bordering the "petit rift" [79] were analyzed by [80] and found to exhibit little reaction with the basaltic host rock in the east. These fluid–rock interactions increase westward toward the western springs. This study also highlighted a water transit time of several years between Ghoubbet and Lake Asal. The Korili spring (Figure 4), which is the westernmost and hottest spring, is fed by water that transits through major fault J, near the Asal 1, Asal 2, Asal 3, and Asal 6 boreholes; this spring also exhibits the strongest fluid–basalt interaction [80]. Lake Asal is enriched in Mg^{2+} and SO_4^{2-} and depleted in Ca^{2+} and Li^{+} relative to the wells (Table 2).

Table 2. Water compositions from Lake Asal and Asal wells. Concentrations are in mg/L. (1) [88]; (2) [91]; (4) [80].

Site	pH	Na	K	Ca	Mg	HCO_3	Cl	SO_4	SiO_2	Li	B	F	NH_3
Deep Reservoir Water													
A3 (4)	5.2	24,900	4830	15,900	24.6	-	70,100	19.1		-	7.7	2.3	-
A3 (2)	-	29,200	5030	17,035	22.9	335	78,425	11		15.3	10.1	9.8	-
A1 (4)	-	28,520	4888	16,389	24.3	-	78,100	21.1		13.2	6.5	-	-
A6 (1)	5.0	25,822	4052	13,375	21.7	-	66,776	7.9	510	-	8.7	2.7	5.8
A4 (4)	5.1	32,200	5318	17,511	2.4	-	85,200	26.9	-	15.2	7	-	-
Lake Asal (1)	7.1	101,200	5161	2677	12500	184	199,155	4320	-	6	-	-	-

2. Materials and Methods

2.1. In the Field

Gas, water, rock, and soil sampling were carried out in the Asal Rift in November 2019 and March 2021. The various sampling sites were determined based on previous ODDEG fieldwork and the existing literature, and by identifying areas with advanced alteration. As the number of roads is limited in this remote area, only sampling sites that were accessible within a day's walk were selected. Some elements of gas composition were measured in situ, while others were measured in the laboratory. Samples were taken from fumaroles in altered rocks, others in open fractures; gas samples were also collected in the form of bubbles in springs (Figure 5); and soil samples were taken near geothermal wells.

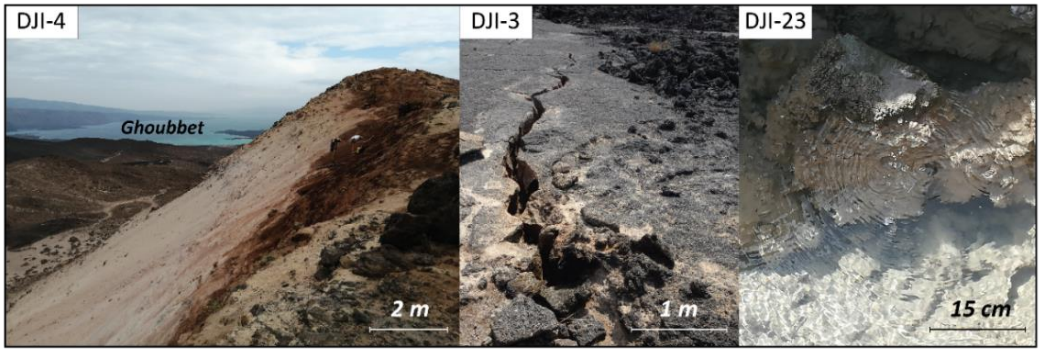

Figure 5. Photos of different sampling sites: fumaroles in highly altered rocks (DJI-4), a fumarole in an open fracture in basalt (DJI-3), and gas bubbles in a spring (DJI-23).

2.1.1. Gas Sampling

The soil layer is thin or missing in Afar, where the volcanic rocks are young and the prevailing climate dry. Accordingly, it can be difficult to perforate the outcropping basaltic rocks. However, fracture networks are widely developed, providing preferential pathways for sampling (see site 3 in Figure 5).

Where geological conditions and geometric constraints (e.g., fracture width) allowed, the bottoms of open fractures were drilled to install a perforated rod for analysis (Figure 6). The stainless-steel rods were designed to sample gases in soils or fractures and were either 40 or 80 cm long. The rods were closed at one end (the lower end) to prevent obstruction of the stem with soil. Near the closed end, holes were made to allow gas flow from the substratum to the collection device. A perforator was used to drill holes with the same diameters as the rods to allow pipes to be inserted. A three-way valve (Swagelok SS-42GXS4) was positioned at the top of the rod. This valve was connected to the analyzer tool using flexible plastic tubing. However, fracture networks in basaltic lavas can be very extensive and may be connected to lava tunnels. In such cases, deep gas concentrations can be considerably diluted in the atmospheric air that circulates in the fracture network.

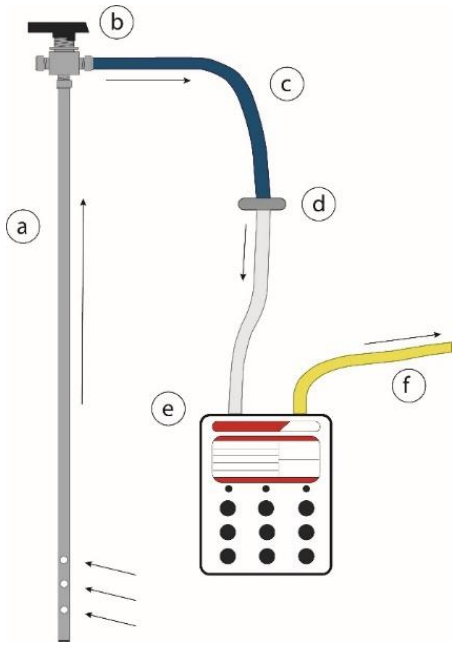

Figure 6. Experimental setup for gas sampling using a stainless-steel rod: (**a**) perforated stainless steel rod; (**b**) three-way valve; (**c**) flexible plastic tubing (inlet); (**d**) waterproof Teflon water vapor filter; (**e**) gas analyzer tool; (**f**) flexible plastic tubing (outlet).

Gaseous emanations from soils are often characterized by zones of concentric alteration where they emerge, with alteration including clays, oxides, and sulfides. In such cases, our protocol (Figure 7) was as follows.

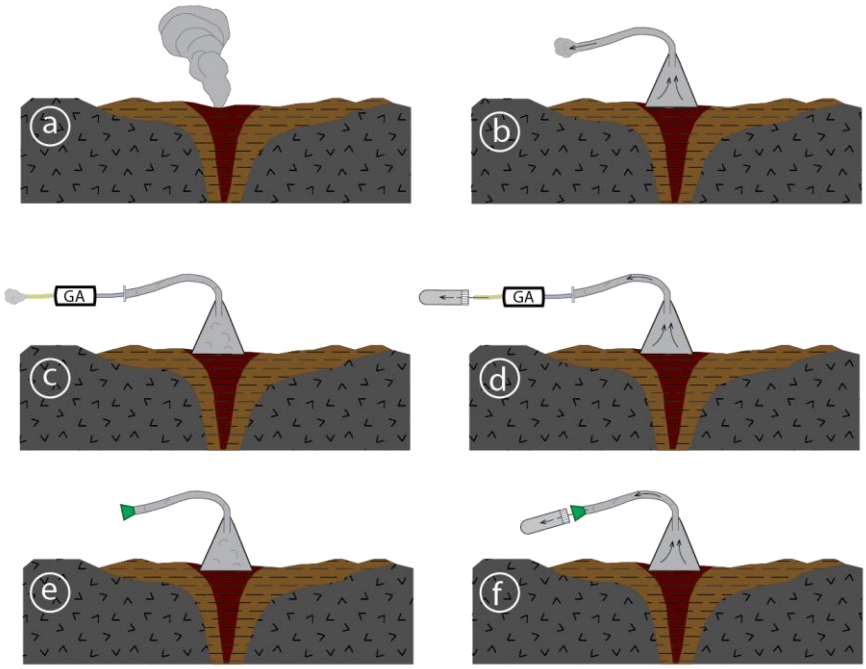

Figure 7. Gas measurement and sampling setup. (**a**) Fumarole system; (**b**) flushing step, with a silicone funnel on the fumarole; (**c**) measurement step, with the measurement tool connected to the collection device and the pump started; (**d**) sampling step, with the needle inserted at the outlet of the measuring tool and the gas collected in vials; (**e**) sampling without the pump, after the flushing step, with the septum at the end of the silicone pipe; (**f**) needle inserted into the septum and gas collected in vials.

First, the soil temperature was measured directly in the soil a few centimeters from the surface, using a probe with a stainless-steel stem or an infrared thermometer, which was placed in the gas or at the epicenter of the emanation (Figure 7a). At the point closest to the emanation, the weathering is typically indicative of higher temperatures, with temperatures decreasing toward the periphery.

Next, a silicone funnel was placed over the emanation (Figure 7b). The advantages of this funnel-shaped bag include its flexibility and malleability, which allow gases to be sampled in confined spaces or areas of complex geometry. The device was left in place for several seconds (or one to two minutes, depending on the flow rate of the emissions) to expel the air in the funnel and tubing.

Then, a waterproof Teflon filter was placed in the middle of the tubing to prevent contact between the water vapor and the sensitive analyzer. Similarly, an H_2S filter can be installed after the steam filter. Once the recollection system was in place, the analyzer tool could be connected (Figure 7c). The pump was started and allowed to run for two minutes (the pump can be restarted manually afterward). This allowed the gas phase to circulate through the device, even at low flow rates.

When gas concentrations increased significantly (typically after 20–30 s, depending on the flow rate), a double-inlet needle (Fischer; 10505444; Greiner Bio-One 450076; 3.81 cm; 21 g; stainless steel) was used to connect the outlet tubing of the analyzer to a glass vial under vacuum to collect the gas (Figure 7d). The vial was allowed to collect gas for approximately 1 min. Two more vials were then used to collect triplicates, one of which was 20 or 12 mL and the other of which was 5.9 mL. The Labco Exetainer®-type vials, sealed and under vacuum, were equipped with a butyl septum to make them impermeable to H_2. This device provided some indication of gas concentrations, via the analyzer, during sampling. Instead of putting the whole assembly in place when the flow was sufficient, a septum plug was placed at the outlet of the funnel or first casing once the air was expelled (Figure 7e).

When the accumulation of gas in the funnel was deemed to be sufficient, based on visible inflation of the bag, the septum plug was pierced with a double needle before attaching a sample vial (Figure 7f). Again, this sampling procedure continued for approximately 1 min or more, depending on the flow rate.

2.1.2. Field Gas Analysis

Geotech's BIOGAS 5000 is designed for in situ gas analysis. This analyzer, equipped with a pump, was used to measure the gas composition of the soils. In this instance, the gases measured were methane (CH_4, %), carbon dioxide (CO_2, %), oxygen (O_2, %), hydrogen (H_2, ppm), carbon monoxide (CO, ppm), and hydrogen sulfide (H_2S, ppm); and finally, the balance was measured in % corresponding to the remaining non-analyzed gases. These measurements are non-destructive: the gas simply circulates through cells in the apparatus before being expelled. Between each measurement, the apparatus was purged to fully evacuate the gas measured previously.

CH_4 and CO_2 are analyzed in the tool using a dual-wavelength infrared sensor with a reference channel. This sensor determined the absorption of infrared light by the gas present in the tool. The gas molecules considered absorb light at different frequencies. Thus, the greater the measured absorption of a certain frequency of light, the higher the concentration of the associated gas.

We analyzed O_2, CO, H_2, and H_2S using internal electrochemical cells. An electrochemical cell consists of a sensing electrode, a reference electrode, a counter electrode, and a liquid electrolyte. As the gas flows through the cell into the electrolyte, it is oxidized or reduced and produces a flow of electrons from the sensing electrode to the counter electrode (the inverse occurs for reduction reactions). The greater this electron flow, the greater the concentration of the associated gas.

The measurement range for CH_4 and CO_2 was 0–100%, with an accuracy of $\pm$0.5%. The measurement range for O_2 was 0–25%, with an accuracy of $\pm$1.0%. In contrast, the

measurement range for H_2, CO, and H_2S, was 0–1000 ppm, with accuracy of ±2.5%, ±2.0%, and ±2.0%, respectively.

Interference can occur between H_2 and CO; where this occurred, the CO value was corrected if this value was less than 1% of the H_2. The measurement of H_2S can also be affected by other gases, causing discrepancies of up to 20% for both SO_2 and NO_2. Similarly, methane values can be overestimated if other hydrocarbons are present in the gas mixture; however, this was not the case in Djibouti.

2.2. In the Laboratory

2.2.1. Laboratory Gas Analysis

Analysis of the sampled gases began with determination of the relative compositions of the mixtures by gas chromatography (GC). This process involved separating and analyzing the gas mixture by increasing the temperature. The gas was split within two capillary separation columns at injection; one was filled with N_2 carrier gas to analyze H_2 and He, while the other was filled with He to analyze the other gases. The gases were differentiated based on their different retention times in the capillary column. Each measurement took approximately 30 min. Two main detectors were used: a flame ionization detector (FID) and a thermal conductivity detector (TCD). The FID detects the ions formed during the hydrogen combustion of organic compounds; these ions are mainly light hydrocarbons. The TCD detects differences in thermal conductivity between the carrier gas and the measured gas. In our study, the measured gases were as follows: H_2, He, CO_2, CH_4, C_2H_6, C_3H_8, i-C_4H_{10}, n-C_4H_{10}, O_2, and N_2.

Once the relative gas compositions were established, δ^2H and $\delta^{13}C$ isotopic measurements were carried out by gas chromatography coupled to a gas source isotope ratio mass spectrometer (GC–C–IRMS, Thermo Mat253). The analytical method varied depending on whether carbon or hydrogen was being analyzed. First, the injected gas was passed through the GC column, where the gases were separated. To analyze for carbon, the gas was then passed through an oven at 1000 °C, which induced combustion and oxidized the carbon-bearing molecules to CO_2. To analyze hydrogen, the gas was passed through an oven at 1420 °C, which induced pyrolysis and reduced the H-bearing molecules to H_2. After exiting the oven, the oxidized or pyrolyzed gas mixture was sent to the IRMS, where it was ionized by an electron; the charged particles were separated by the magnetic sector and only particles with a defined mass to charge ratio were able to reach the detector. The detector converted the particles into an electrical signal and amplified the signal. Finally, the software processed the data and calculated an isotopic ratio. Values for the CO_2 internal reference gas used to calibrate each measurement were determined using multiple IAEA carbonate standards (IAEA-603, 610, 611, 612) on an EA–IRMS device. For the GC–C–IRMS, the efficiency of hydrocarbon oxidation and pyrolysis into CO_2 or H_2 was checked before each analytical session by injecting, as a sample, two different commercial external methane isotopic standards (such as Air Liquide Thermo 1.2 and Air Liquide Bio 1.0 gases). If the analytical values of the commercial standards were within 0.1‰ of their independently determined values, the combustion process was deemed valid and without fractionation. The samples collected in the field were then analyzed.

2.2.2. Rock and Alteration Mineral Sample Analysis

Rocks and alteration minerals were collected at field sites of interest, where hydrogen was detected in the gas phase. Various analyses were conducted, including bulk analyses of powders produced from the samples (X-ray diffraction, or XRD, and Mössbauer spectroscopy) and the preparation of thin polished sections of 30 µm for in situ analyses (microscope, scanning electron microscope or SEM, and microprobe).

The bulk analysis of powder allowed us to determine the mineralogical compositions of the samples. The XRD analyses were carried out with a D2 PHASER (Bruker) diffractometer. This allowed for qualitative and quantitative analysis and provided information about the crystalline phases present. X-rays were projected onto the powder samples and

the intensities of the diffused X-rays were analyzed according to the orientations. The non-crystalline clay phases had to undergo preliminary preparation to obtain an identifiable signal. First, the clay powder was suspended in a tube filled with distilled water. To avoid any flocculation, two drops of ammonia were added. After shaking, the newly oriented powder was deposited on glass slides. Three slides were analyzed for each sample: the first was analyzed as it was, the second after addition of ethylene glycol to identify swelling clays, and the third after the sample had been passed through the oven at 500 °C to observe retraction phenomena. Analyses were undertaken at 10 mA, 300 W, and 30 kV with a PSD of 1.6 s and 0.2/1.0/3.0 mm slots. The analyses proceeded from 2° to 40° 2θ, with 1.54184 X-ray wavelengths. Bragg's law was used to determine the inter-reticular distances between the clay layers based on X-ray diffraction, where:

$$2d_{(hkl)} \times \sin(\theta) = n \times \lambda \quad (1)$$

- $d_{(hkl)}$: inter-reticular distance (in Å)
- θ: Bragg angle or half angle of deviation
- n: diffraction order
- λ: X-ray wavelength (1.54184 Å)

Analyzing the valency of transition metals within the rock can provide information that is essential to addressing some of the main issues facing research into natural hydrogen production, particularly those relating to its origin and formation mechanism. One potential source of natural hydrogen is the redox reaction between ferrous iron (i.e., the Fe^{2+} contained in minerals) and water, to form both ferric iron (Fe^{3+}) and H_2. Thus, after identifying the crystalline and non-crystalline phases of our samples by XRD, we measured iron (II) and iron (III) contents by Mössbauer spectroscopy of ^{57}Fe. These analyses, undertaken at the ICMCB (University of Bordeaux) in the "Resonance Spectroscopy" department, were performed on a Halder-type spectrometer with constant acceleration. This analysis is based on the absorption of gamma rays by the atomic nuclei of a solid, emitted on the powder. The radioactive source (^{57}Co) was maintained at room temperature (293 K). At the exit, a detector measured the transmitted intensity.

Finally, microscopy allowed the identification of the different primary and alteration minerals and the matrix for the thin sections. Following these observations, SEM analyses were performed at ISTeP using a ZEISS Supra 55 VP SEM and "Schottky"-type field effect gun with a variable pressure chamber, and an EDS analysis system QUAD de BRUKER with 4 crystals Silicon Drift Detector. A voltage of 15 kV was applied for these analyses to produce images in the angle-selective backscatter (AsB) mode. These analyses are relative; accordingly, microprobe analyses were carried out to obtain quantitative values for the different primary and secondary minerals.

The microprobe analyses were performed at the Raimond Castaing Microcharacterization Center in Toulouse (CNRS). The electron microprobe was a CAMECA SXFive. This method is non-destructive. Punctual analysis of major elements, for basalts and alteration minerals, was performed under conditions of 20 keV and 20 nA for a beam size of 1 µm. Thin sections were analyzed for rocks from the same site (DJI-4), including a plagioclase porphyry basalt and the altered basalt, for a total of 400 measurement points. The oxides measured were SiO_2, TiO_2, Al_2O_3, FeO, MgO, MnO, CaO, Na_2O, K_2O, NiO, and Cr_2O_3.

3. Results

3.1. Surface H_2 Emanations

During the field campaign in November 2019, a long cross-section was prospected. This section extended from Obock in the north, near the accretionary center of the Aden Ridge, to Lake Abhe in the southwestern part of the Goba'ad graben (Figure 3). Twenty-five sites were sampled, representing the variety of large structures in the region: the chimneys of Lake Abhe, the grabens of Hanle and Gaggade, the Asal Rift, the North Ghoubbet zone, and near the spreading axis of the Aden Ridge (Tadjoura and Obock).

The sites between Obock and Lake Abhe were measured using the BIOGAS 5000 and were selected based on the presence of surface markers, such as fumaroles, unusual clayey zones, hot springs, or carbonates in basalts. Where possible, measurements were also obtained within the rift faults (both active and inactive) or near various geothermal wells.

In August 2020, two additional days of gas field measurement were undertaken at two sites in the Asal Rift; these sites were previously identified as the most promising according to their H_2 concentration.

As shown in Figure 8, the sites with significant H_2 concentrations are located in the center of the Asal–Ghoubbet Rift; more precisely, they lie along the internal margin (red dots in Figure 8). This is evidenced by site 4, which is located on major fault F, southwest of the Fiale Caldera (location: Figure 4, photo: Figure 5). This site is a fumarole with high surface temperatures (96 °C). The North Ghoubbet area, despite exhibiting high surface temperatures (97 °C) and many important geothermal markers (i.e., at sites 8, 9, and 10), does not exhibit high H_2 concentrations in the soil or fumaroles (Table 3). Similarly, in the Gulf of Tadjoura, along the margins of the Aden Ridge, no evidence of H_2 was found, despite the existence of hot springs. Furthermore, no high H_2 concentrations (i.e., above 200 ppm) were found in the three southern grabens of Hanle, Gaggade, and Goba'ad during the first survey, despite surface evidence of fumaroles (location: Figure 3). However, the intense hydrothermal alteration in the Gaggade graben, and the presence of springs with bubbles and travertine chimneys at Lake Abhe [93], prompted us to collect additional data.

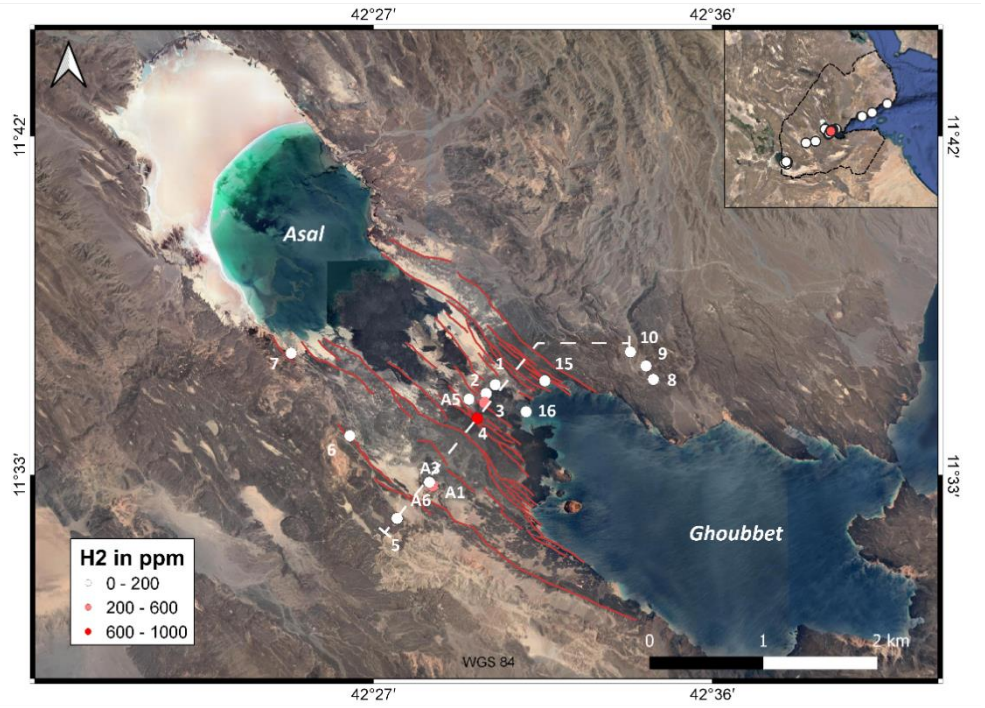

Figure 8. Satellite map of H_2 emanations in the Asal–Ghoubbet Rift. Locations of measurement sites are shown along with their in situ H_2 concentrations (in ppm) before air correction. Inset map illustrates H_2 repartition in the Republic of Djibouti, oriented along a NE–SW axis. Cross-section of the Figure 17 in white dashes.

Table 3. Non-corrected gas concentrations from field measurements. F: fumaroles; S: soil; S/W: soil near a geothermal well. (0): Standard deviation between n measurements from the same site. Where this value is 0, the n values were identical.

	Site	Cat.	n	CH_4 %	CO_2 %	O_2 %	H_2 ppm	CO ppm	H_2S ppm	Bal. %
Asal–Ghoubbet	DJI-1	S/W	1	0.0 (0)	0.1 (0.0)	19.4 (0.0)	68 (0)	2 (0)	1 (0)	80.5 (0)
	DJI-2	S/W	1	0.0 (0.0)	0.0 (0.0)	19.0 (0.0)	20 (0)	0 (0)	1 (0)	81.0 (0)
	DJI-3	F	10	0.0 (0.0)	2.6 (1.5)	19.3 (0.4)	77 (60)	2 (0)	1 (0)	78.2 (1.2)
	DJI-3	F	5	0.0 (0.0)	2.5 (1.4)	18.7 (0.6)	107 (77)	2 (0)	7 (1)	78.8 (1.2)
	DJI-4	F	14	0.0 (0.0)	4.4 (0.8)	19.3 (0.3)	540 (125)	2 (2)	1 (1)	76.3 (0.7)
	DJI-4	F	13	0.0 (0.0)	3.4 (0.7)	18.6 (0.3)	829 (134)	4 (3)	36 (8)	77.9 (0.6)
	DJI-4	F	22	0.0 (0.0)	1.9 (0.4)	19.7 (0.7)	537 (96)	3 (2)	29 (6)	78.4 (0.5)
	DJI-5	S	4	0.0 (0.0)	0.6 (0.3)	19.9 (0.1)	2 (2)	0 (0)	1 (0)	79.5 (0.3)
	DJI-6	F	2	0.0 (0.0)	0.1 (0.1)	20.0 (0.0)	0 (0)	0 (0)	1 (1)	80.0 (0.1)
	DJI-8	S	3	0.0 (0.0)	0.2 (0.2)	19.7 (0.2)	15 (9)	0 (0)	1 (0)	80.1 (0.2)
	DJI-9	F	3	0.0 (0.0)	0.6 (0.4)	19.9 (0.1)	4 (0)	0 (0)	1 (0)	79.7 (0.3)
	DJI-10	S	3	0.0 (0.0)	0.4 (0.3)	19.9 (0.1)	2 (1)	0 (0)	1 (0)	79.6 (0.2)
	DJI-15	S	4	0.0 (0.0)	0.0 (0.0)	20.0 (0.0)	2 (1)	0 (0)	1 (0)	80.0 (0.0)
	Asal 3	S/W	4	0.0 (0.0)	0.1 (0.1)	20.1 (0.4)	35 (22)	6 (5)	2 (2)	79.9 (0.4)
	Asal 1	S/W	6	0.0 (0.0)	0.2 (0.2)	20.0 (0.6)	138 (85)	8 (4)	1 (1)	79.9 (0.5)
	Asal 6	S/W	3	0.0 (0.0)	0.2 (0.1)	19.7 (0.1)	83 (48)	4 (1)	1 (0)	80.1 (0.1)
	Asal 5	S/W	2	0.0 (0.0)	0.1 (0.0)	20.7 (0.1)	0 (0)	0 (0)	0 (0)	79.0 (0.1)
	DJI-13	S	1	0.0 (0.0)	0.1 (0.0)	19.9 (0.0)	1 (0)	0 (0)	1 (0)	80.0 (0.0)
	DJI-14	S	1	0.0 (0.0)	0.1 (0.0)	19.8 (0.0)	1 (0)	0 (0)	1 (0)	80.1 (0.0)
	DJI-19	F	1	0.0 (0.0)	0.1 (0.0)	19.6 (0.0)	52 (0)	0 (0)	1 (0)	80.3 (0.0)
	DJI-21	S	5	0.0 (0.0)	0.0 (0.0)	19.2 (0.4)	43 (52)	5 (1)	1 (0)	80.7 (0.4)
	DJI-22	S	3	0.0 (0.0)	0.2 (0.2)	19.2 (0.5)	5 (2)	3 (0)	1 (0)	80.6 (0.3)

Here, we focus primarily on analysis of the samples from site 4 in order to constrain the mineralogical and chemical characteristics of the rocks associated with this site. These results will allow us to explore the reactions from which the measured H_2 may have arisen.

3.2. Site 4

Site 4 is located on the footwall of major fault F (Figure 4). Various lithologies were observed at this site, where porphyritic basalts with plagioclases were found to underlie lavas with aphyric characteristics. The contact zone between these two units is very clayey, forming an altered, initially permeable scoriaceous interflow zone. We observed hydrothermal manifestations at the surface, numerous fumaroles at temperatures up to 96 °C, and hot water condensation shelters installed by the Afar pastoralist population.

3.2.1. Gas

In situ H_2 concentrations were found to exceed 1000 ppm at times in the fumaroles, with CO_2 values up to 5.8% (Figure 9). However, CO_2 and H_2 values were lower both above and below the emissive zone; these values were in the ranges 0–3% and 0–250 ppm, respectively, depending on proximity to the emissive zone (considered at distances of 1–5 m). No methane was detected. Oxygen was ubiquitous, with concentrations of 17–20%, which we attribute to the air contamination discussed previously. We found H_2S concentrations here to be negligible. The balance (i.e., the portion comprising the remaining non-analyzed gases) was made up by N_2 for the most part. Therefore, assuming that all O_2 present came from a source outside the system, and that removing this oxygen removed the equivalent volume of atmospheric N_2 (according to the ratio $N_{2(atm)}/O_{2(atm)}$ = 3.727), we concluded that the remaining non-analyzed gas represents nitrogen coming from deep within the system. To be more accurate, we also remove the argon component of the air in the same way, based on the ratio $Ar_{(atm)}/O_{2(atm)}$ = 0.044. Based on these calculations,

we estimated these gases to represent only 2–13% of the overall composition of the samples, and used our results to calculate the relative concentrations of the gases of interest (Table 4).

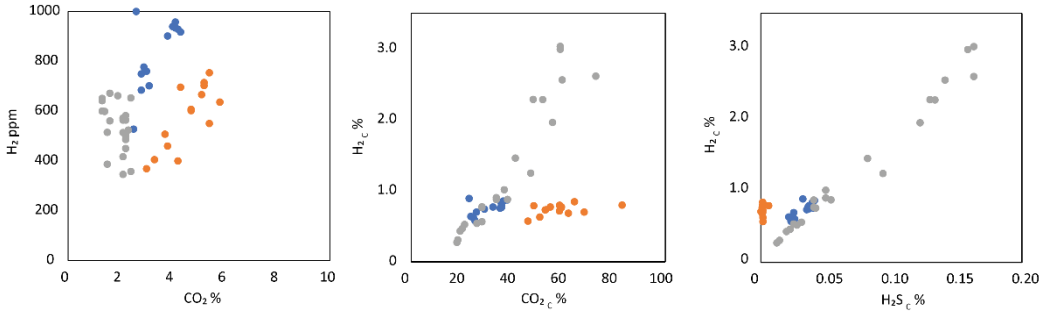

(**a**) (**b**) (**c**)

Figure 9. Diagram illustrating gas concentrations for the DJI-4 fumarole. (**a**) Non-corrected gas with H_2 in ppm versus CO_2 in %. (**b**) H_2 (%) versus CO_2 (%) after air correction. (**c**) H_2 (%) versus H_2S (%) after air correction. Measurements were obtained on 21 November 2019 (orange dots), 12 August 2020 (blue dots), and 13 August 2020 (gray dots).

Table 4. Average air-corrected gas compositions from the site 4 field measurements. F: fumaroles; n: number of measurements.

Site	Cat.	Date	n	CH_4 c %	CO_2 c %	H_2 c %	CO c %	H_2S c %	Bal. c %
DJI-4	F	21 November 2019	14	0.0 (0)	56.0 (9.0)	0.7 (0.07)	0.009 (0.002)	0.002 (0.001)	43.3 (9.1)
DJI-4	F	12 August 2020	13	0.0 (0)	30.6 (5.4)	0.8 (0.1)	0.002 (0.005)	0.03 (0.01)	68.6 (5.5)
DJI-4	F	13 August 2020	22	0.0 (0)	38.2 (15.7)	1.3 (0.9)	0.02 (0.02)	0.07 (0.05)	60.4 (16.7)

After these corrections, H_2 concentrations were up to 3%, and the maximum concentration of CO_2 was 83%. No clear trend was evident in our raw data; however, a positive correlation between H_2, CO_2, and H_2S concentrations is evident in the corrected data (Figure 9). This correlation is even stronger for samples collected on the last day. After correction of gas compositions, the remaining gas (primarily N_2) was still an important phase of the gas mixture.

The GC gas composition results (i.e., 20.8% O_2) underline the presence of atmospheric gas in the system. Our raw data are consistent with previous in situ measurements. After applying the correction methods described above, we obtained H_2 values that correspond broadly to the average values calculated in previous studies (Table 5). Our results also indicate CO_2 concentrations that are typical for this setting. The sulfur species present could not be determined, but an unidentified peak (for which we had no standard) can likely be attributed to H_2S.

Table 5. Gas chromatography data from site 4, including non-corrected and air-corrected measurements.

Site	Cat.	He %	CH_4 %	CO_2 %	H_2 %	O_2 %	N_2 %	Unknown %
DJI-4	F	-	0.002	5.2	0.06	20.8	75	0.005
DJI-4 c	F	-	0.04	84.9	0.9	-	14.1	0.08

The high H_2O contents of the sampled gas coupled with the high dilution of H_2 by air in the samples did not allow for conclusive δD and δC values.

Having confirmed the presence of H_2, we then investigated the characteristics of the bedrock at the site to better understand potential fluid–rock interactions.

3.2.2. Microscopy

The unaltered plagioclase porphyritic basalt sample (Figure 10a) exhibits high porosity (in the range of 30%). Two phases can be distinguished based on microscopic observations: porphyric minerals (70%) and mesostasis (30%). The automorphous primary minerals are 95% plagioclase feldspars (several cm long), 3% olivines (several mm long), and 2% clinopyroxenes (several mm long). The olivines, often in aggregates, are found mostly at the edges of the plagioclases and exhibit iddingsite forms (Figure 11a,b). Clinopyroxene, although present as crystals, is also visible as exsolution lamellae in the plagioclases. Many fluid inclusions are present in these plagioclases Figure 11c). The mesostasis, mostly gray, is composed of micrometer-sized crystals of plagioclase, olivine, clinopyroxene, and various oxides and apatites.

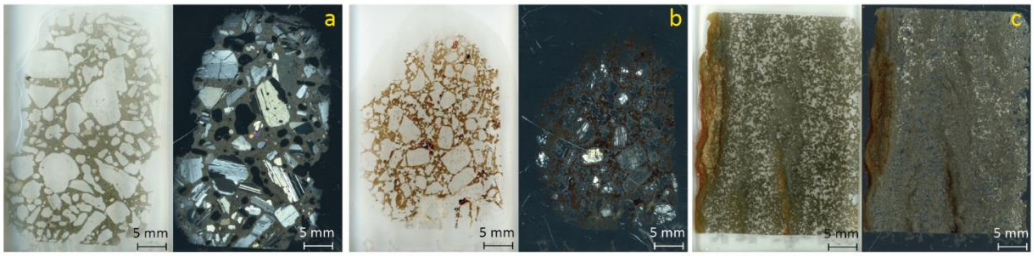

Figure 10. Thin section scans in LPA and LPNA from site 4. (**a**) Porphyritic basalt with plagioclase DJI-4-13. (**b**) Altered porphyritic basalt with plagioclases DJI-4-1. (**c**) Aphyric lava DJI-4-12.

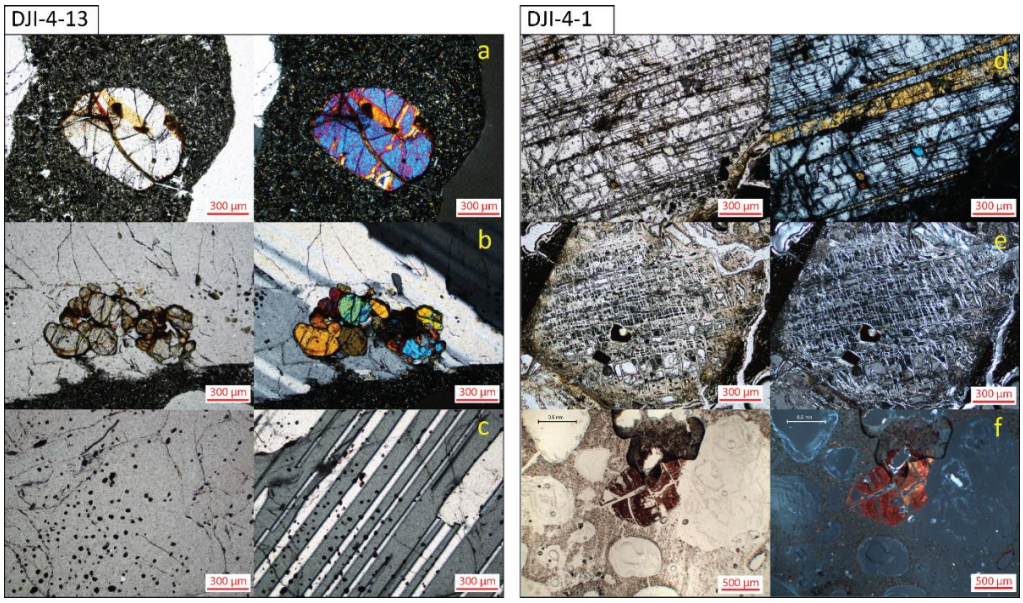

Figure 11. Close-up views of thin sections in natural light and polarized light. DJI-4-13 (fresh basalt): (**a**) olivine crystal showing multiple fractures and iddingsite forms; (**b**) olivine aggregate in a plagioclase with iddingsite forms; (**c**) multiple fluid inclusions in plagioclases. DJI-4-1 (altered basalt): (**d**) partially altered and densely fractured plagioclase with some unaltered clinopyroxenes; (**e**) plagioclase completely altered in clay showing a fracture network corresponding to and perpendicular to the original polysynthetic macle; (**f**) Mn-Fe oxide between the relics of plagioclase crystals.

The altered plagioclase porphyritic basalt samples (Figure 10b) show a porosity up to 50% and are poorly consolidated: they are prone to crumbling when touched. These

samples are brown–orange in color. Under the microscope, we observed plagioclases partially or totally altered (Figure 11d,e). Moreover, these plagioclases are more closely packed than those in the unaltered basalt. No olivines or clinopyroxenes are visible. Many oxides (Figure 11f) and inclusions are also present. Less than 10% of the primary minerals remain unaltered.

Finally, the aphyric lava samples (Figure 10c) exhibit very low porosity. The minerals in these samples are not directly visible or identifiable.

3.2.3. SEM

SEM backscattered electron imaging allowed us to highlight variations in the chemical elements of the minerals considered, particularly the transition metals including Fe, Ni, Mn, and Ti. These variations help to identify the zones in which oxides are concentrated or where zonations are present in the minerals.

The matrix of the fresh basalt sample (DJI-4-13) is composed of plagioclase (100 µm long), clinopyroxene (40 µm), olivine (40 µm), titano-magnetite (50 µm), and ilmenite (50 µm). The olivine phenocrysts exhibit zonation, with iron enrichment at their edges (Figure 12a); this feature was apparent under the microscope, with iddingsitization of the olivines. The olivines present in the matrix represent the most iron-enriched phases. In contrast to the more isolated olivines in the matrix (Figure 12b), those near the more porous zones exhibit flame-like bodies of hematite enrichment in forsterite (Figure 12c). This kind of Fe enrichment was described previously by [94].

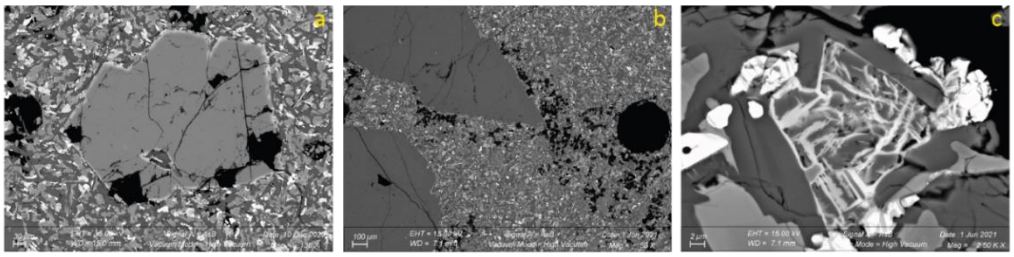

Figure 12. DJI-4-13 SEM pictures in AsB mode displaying (**a**) Fe zonation at the edges of macroscopic olivines and Fe-Ti-rich oxides in the matrix; (**b**) concentration of porosity along and behind centimeter-scale plagioclase minerals, with zones of Fe enrichment textures in olivines; (**c**) flame-like bodies of hematite in an Mg-olivine close to the area of porosity.

In sample DJI-4-1, which has been intensely altered, only a few plagioclases are not fully altered (Figure 13a). Very fractured millimeter-scale oxides of iron and manganese are also evident. The matrix is strewn with very rich iron and titanium oxides that are approximately 10 µm in size (Figure 13b). Few other minerals are visible, although Mn-oxides (Figure 13c) are apparent in the matrix, which is essentially clay-like. The compositions of the altered plagioclases are closer to kaolinite (where the Si/Al ratios are between 0.8 and 0.9), whereas the matrix is closer to a smectite (with Si/Al ratios between 0.5 and 0.7).

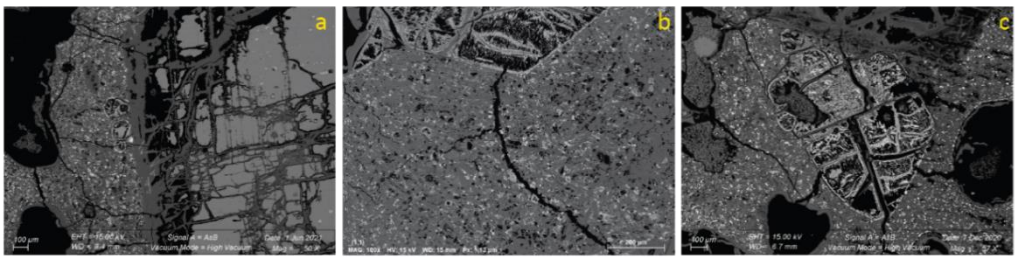

Figure 13. DJI-4-1 SEM pictures in AsB mode displaying (**a**) a centimeter-scale plagioclase partially altered to kaolinite/smectite with an olivine next to it in a smectite and oxide matrix; (**b**) close-up view of the iron-rich smectite matrix near a Mn-oxide; (**c**) fractured Mn-oxide with white Fe enrichment.

The aphyric lava (DJI-4-12), which is not very porous, exhibits a mineral assemblage composed primarily of plagioclase (100 µm long), followed by xenomorphic olivine (40 µm), clinopyroxene (40 µm), ilmenite (50 µm) and titano-magnetite (50 µm).

3.2.4. XRD

XRD was performed only on the altered basalt sample to define the associated alteration clays. The XRD signal from the basic DJI-4-1 exhibits a phase with a peak at 6.10 (2θ). After mixing with ethylene glycol and oven drying, the sample produced peaks at 5.47 (2θ) and 9.52 (2θ), respectively. Using Bragg's law (Equation (1)), we obtained inter-reticular distances ($d_{(hkl)}$) of 14.48, 16.13, and 9.29 Å for the unprocessed sample, the sample treated with ethylene glycol, and the oven-dried sample, respectively (Figure 14). These distances suggest that the clay phase present is a smectite-rich mixed-layer mineral [95]. In contrast, peaks in the range 20–40 2θ° are indicative of different Fe-Ti-oxides.

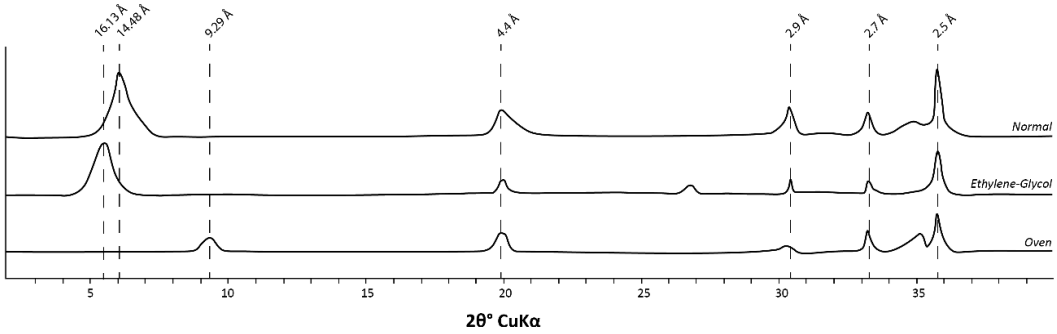

Figure 14. XRD signals obtained for sample DJI-4-1 (altered sample). Three signals are shown, for the unprocessed clay sample, the sample after ethylene glycol pulverization, and the sample after oven drying at 500 °C.

3.2.5. Mössbauer Spectroscopy ^{57}Fe

Various phases were identified in the unaltered sample (DJI-4-13): three Fe (III) phases, three Fe (II) phases, and a mixed phase. These phases can be present as tetrahedral or octahedral forms, whether ferrous or ferric iron.

The proportions of different phases (as determined by integrating the peak signals) can be subject to large uncertainty because the analyses were performed at room temperature. Nevertheless, such analysis allows comparison of Fe (II) and Fe (III) between different samples. By summing the different iron valencies, we were able to obtain Fe^{2+}/Fe^{3+} ratios (Table 6). For the fresh basalt sample (DJI-4-13), this ratio was 35% Fe^{3+} and 65% Fe^{2+}. For the aphyric lava sample (DJI-4-12) and the altered basalt sample (DJI-4-1) we obtained Fe^{2+} (Fe^{3+}) values of 76% (24%) and 10% (90%), respectively. The majority of ferric iron is typically assimilated to ferrihydrite [96,97]. Ferrihydrite is an unstable, poorly crystalline oxyhydroxide of hydrated octahedral ferric iron; its chemical formula is $Fe^{3+}{}_5O_8{\cdot}nH_2O$ [98].

Table 6. Mössbauer spectroscopy from ^{57}Fe analysis of site 4 samples: fresh basalt, altered basalt, and aphyric basalt.

Sample	A1	δ (mm/s)	Δ (mm/s)	B_{hf} (T)	Γ (mm/s)	Area (%)	Attribution	Minerals
Fresh Basalt (DJI-4-13)	DQ1	0.37	0.71	-	0.30	10	Fe^{3+} oct.	Olivine/Iddingsite
	DQ2	0.94	0.84	-	0.60	10	Fe^{2+} tet.	Ilmenite
	DQ3	1.14	1.99	-	0.44	35	Fe^{2+} oct.	Clinopyroxene
	DQ4	1.14	2.89	-	0.32	21	Fe^{2+} oct.	Olivine
	S1	0.36	−0.23	50.4	0.60	10	Fe^{3+}	Maghemite/Hematite
	S2	0.29	−0.09	49.3	0.70	7	Fe^{3+} tet.	Magnetite
	S3	0.61	−0.02	45.5	0.70	7	$Fe^{2+/3+}$ oct.	Magnetite
Altered Basalt (DJI-4-1)	DQ1	0.36	0.74	-	0.48	48	Fe^{3+} oct.	Ferrihydrite/Smectite
	DQ2	0.95	1.04	-	0.53	6	Fe^{2+} tet.	Ilmenite
	DQ3	1.14	2.76	-	0.50	2	Fe^{2+} oct.	Olivine/Smectite
	S1	0.36	−0.14	50.7	0.46	27	Fe^{3+}	Maghemite/Hematite
	S2	0.27	−0.03	48.5	0.53	11	Fe^{3+} tet.	Magnetite
	S3	0.61	−0.02	44.9	0.54	7	$Fe^{2+/3+}$ oct.	Magnetite
Aphyric Basalt (DJI-4-12)	DQ1	0.39	0.75	-	0.36	10	Fe^{3+} oct.	Olivine/Ferrihydrite
	DQ2	0.99	0.85	-	0.50	11	Fe^{2+} tet.	Ilmenite
	DQ3	1.16	1.98	-	0.43	29	Fe^{2+} oct.	Clinopyroxene
	DQ4	1.17	2.90	-	0.36	35	Fe^{2+} oct.	Olivine
	S1	0.36	−0.22	51.2	0.30	2	Fe^{3+}	Hematite
	S2	0.27	−0.01	49.0	0.66	8	Fe^{3+} tet.	Magnetite
	S3	0.68	−0.13	45.8	0.66	6	$Fe^{2+/3+}$ oct.	Magnetite

We found little variability in magnetite proportions between our samples, with only a slight increase in Fe^{3+}-magnetite in the altered basalt relative to the other samples. In contrast, we found the ilmenite (Fe^{2+}) content to be slightly lower in the altered sample. Relative to the fresh basalt, the proportions of maghemite/hematite (Fe_2O_3) and ferrihydrite in the altered basalt were found to be approximately three and five times greater, respectively. These variations in oxide content reflect enrichment in Fe^{3+} during alteration, during which the Fe^{2+}-rich primary minerals disappear almost completely. For example, the DQ1 signal is associated with Fe^{3+} in octahedral sites in olivine in the fresh samples, but is associated with ferrihydrite in the altered sample (DJI-4-1), for which SEM images indicate the absence of olivine.

3.2.6. Microprobe

The SEM analyses demonstrated that the olivine phenocrysts in the fresh basalt sample exhibit enrichment of iron toward the rim, from $Fo_{81–76}$ to $Fo_{57–42}$; a similar pattern was also observed for Mn enrichment. The average structural formula of the olivine cores is $(Mg_{1.52},Fe_{0.42})Si_{1.01}O_4$, whereas that of the olivine rims is $(Mg_{0.85},Fe_{1.02})Si_{1.02}O_4$. Furthermore, clinopyroxene phenocrysts in the fresh basalt exhibit compositions enriched in aluminum ($Al_2O_{3\ max}$ = 17.05%) and titanium ($TiO_{2\ max}$ = 15.29 %). As shown in Figure 15a, these clinopyroxenes are essentially augites, but tend toward pigeonites; their average structural formula is $(Ca_{0.61}Na_{0.09}Mg_{0.62}Fe_{0.47}Al_{0.13}Ti_{0.11})(Si_{1.77}Al_{0.2})O_6$.

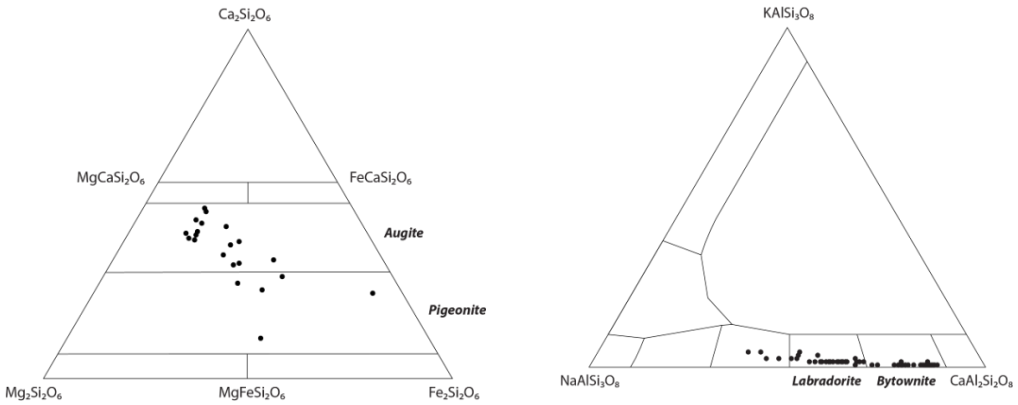

Figure 15. (**a**) Partition of clinopyroxenes from the porphyritic basalt in a ternary diagram between enstatite–wollastonite–ferrosilite endmembers. (**b**) Partition of plagioclases from the porphyritic basalt in a ternary diagram between the albite–orthoclase–anorthite endmembers.

The plagioclases are calcic, with mostly bytownites and some labradorites (Figure 15b). Andesine zonation is also evident, as demonstrated previously by [64,85]. These plagioclases have an average structural formula of $Na_{0.21}Ca_{0.79}Al_{1.68}Si_{2.23}O_8$. Some enrichment in iron and magnesium can be observed in these crystals, although this is rare.

Analysis of the altered sample demonstrated a variable clay composition with phases variably enriched in iron (FeO%). As observed by SEM, the composition of the clay phase present in the semi-altered plagioclases is close to that of a 1:1 kaolinite-type clay, with Al_2O_3/SiO_2 ratios in the range 0.8–0.93. In the matrix, this ratio decreases to 0.5. The FeO% composition (FeO + Fe_2O_3, %) is constant and does not exceed 3% in the kaolinite-type clays, whereas the matrix FeO% values vary significantly and can reach 34%. Based on our ternary diagrams (Figure 16) and considering clay endmembers [99,100], we interpret the kaolinite-type clays to represent a solid solution series between the kaolinite endmember and the beidellite endmember (smectite group); the clay matrix is closer to Fe-beidellite type. It is important to note that the numerous iron oxides (hematite, magnetite, ilmenite, maghemite, and ferrihydrite) scattered in the matrix can affect microprobe measurements.

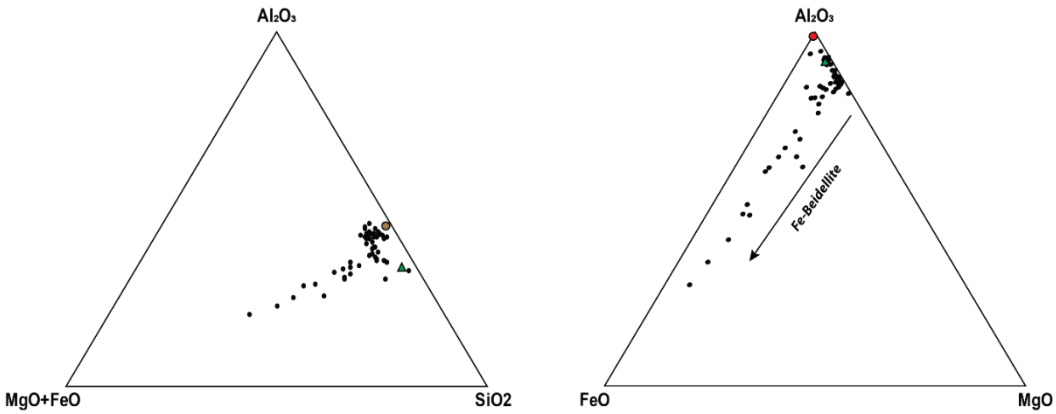

Figure 16. Ternary diagrams illustrating the distribution of clays within the samples. This distribution indicates iron enrichment of the clays toward a Fe-beidellite pole. Kaolinite (pink dot) and beidellite (green triangle) poles are also shown.

4. Discussion

Based on the data collected along our NE–SW transect across the Republic of Djibouti, hydrogen concentrations are highest in the active Asal–Ghoubbet Rift and, more precisely, in the magmatically active axial zone of the rift in the Fiale Caldera area, between major

faults E and F. Along the Aden Ridge, tidal action may have masked potential gas discharge areas. It is also important to note that the distances between our sampling sites and the respective magmatically active segments along the Gulf of Tadjoura–Ghoubbet part of the Aden Ridge are similar to or greater than the distances between the sites located along the Asal margin and the active rift on land. In addition, hydrothermal paleo-deposits were observed on the walls of the east–west faults affecting the Gulf Basalt series, although the numerous rockslides in this area made accessing the foot of the fault scarps impossible. However, the new data presented here and the previously published data do allow us to discuss various issues: the presence of gases in the subsurface, the origins of these gases (e.g., volcanic or due to water–rock interactions within the upper part of the crust), and the migration pathways of fluids. In particular, we were able to define the depths of gas generation and water penetration using geothermometers. As stated previously, the water present in this region is either marine water that flows from Ghoubbet Bay to Lake Asal, or meteoric water.

4.1. Isotope Geothermometers

The δD isotope ratios of the gas collected from borehole A6 [88] indicate an H_2-CH_4 equilibrium temperature between 270 °C and 292 °C according to the reaction equations, and an H_2-H_2O equilibrium temperature of 270 °C. The $\delta^{13}C$ isotopic signatures have been shown to indicate CO_2-CH_4 equilibrium temperatures of approximately 281 °C, 309 °C, and 332 °C for A5, A6, and A3, respectively, based on calculations using Bottinga's (1969) equation for $\delta^{13}CH_4$ and CO_2. These values are in good accord with the δ^2H paleothermometer results for A6. In most of the Icelandic geothermal fields (including Reykjanes, Krisuvik, Hveragerdi, Nesjavellir, Namafjall, Krafla, and Landmannalaugar), the highest H_2 contents in fumarole steams are associated with the highest H_2 geothermometer temperatures, which are typically above 270 °C [45]; this pattern has also been found for CO_2 and H_2S.

Mantle-derived CO_2 has been found in the axial zone or center of the rift under site DJI-4, whereas a mixture of mantle- and sediment-derived CO_2 is present in the outer margins [88,91,92]. The temperature of the geothermal reservoir in the outer margins is approximately 260 °C, which is close to the equilibrium temperature of H_2-CH_4. Except for the deep waters of the geothermal reservoir, no fluids have reached equilibrium with the basalt; accordingly, there is little or no direct contact between surface and deep fluids in this region [79,80]. Well temperature data indicate that the geothermal fluids here fall under the boiling point curve, and increasing the salinity content would increase the boiling point [101]. Thus, the surface fumarole composition in the rift axis can be explained by the addition of mantle CO_2 to the shallow geothermal system (i.e., to the marine water intrusion under the Fiale Caldera), which would reduce the boiling point and induce a pressure disequilibrium to allow steam formation [102]. The Asal geothermal model of [103] illustrates the hypothesis of a vapor-dominated system on the western edge of the Fiale Caldera.

4.2. Mantle Influence on the Gas Mixture

Although hydrogen has been measured in the Asal wells on the outer margins of the rift, we found rather low hydrogen contents at the surface for the nearby sites. CO_2 is the dominant gas phase (excluding water vapor) in the wells. In the DJI-4 fumaroles, the gas phase still had rather low H_2 concentrations after correction for air contamination, and CO_2 remained a major phase of the mixture. The concentration of H_2O could not be constrained, owing to the presence of a water-vapor filter in our sampling system; however, based on our observations, we can infer that water vapor is a major gas in the fumaroles. For example, water condensed in our tubing, and Afar pastoralists have built stone shelters over most fumaroles to condense steam and recover the liquid water that is lacking in this arid area. CO is a mantle-derived gas similar to CO_2 and SO_2. However, as CO was not found in measurable amounts within the fumaroles, we can conclude that either magmatic gases

have limited access to the surface system [102], or that any CO present would have reacted with H_2 to form reduced carbon species through FTT reactions. In addition, SO_2 was the major phase during the Ardoukoba 1978 eruption [92], but was not found in fumaroles during this campaign. This discrepancy can be attributed to our experimental protocol. In particular, our field detector did not measure SO_2; accordingly, it could be the unknown gas analyzed in our GC sample, although its concentration was very low. Mantle-derived SO_2 is extremely soluble [102] and will react with H_2O to form sulfate in aquifers; similarly, CO_2 will react with H_2O to form bicarbonate in aquifers. Indeed, SO_4^{2-} and HCO_3^- have been found in geothermal wells [80,88,91]. We found CH_4 to be a minor phase in both Asal wells and fumaroles. Isotopic data relating to CH_4 are in the limit between thermogenic and volcanic-geothermal systems area [104]. However, as proposed by [105]), post-magmatic reactions could form CH_4 by successive reactions with CO_2, H_2O, and metal oxides at temperatures of 200–500 °C.

The H_2S found in the wells could be mantle-derived or formed by successive reactions with SO_2 gas that was initially mantle-derived, thus producing an $HS^-_{(aq)}$ state that can react with H^+ to form H_2S. $HS^-_{(aq)}$ ions can also react with H_2O to form sulfate, protons, and hydrogen [106]. H^+ ions are abundant in geothermal systems and can be produced by many different reactions [102]. The production of protons in magmatic gases could explain the low pH (4–5) found in the Asal system. Such low pH values can enhance rock dissolution, which can (alongside high-temperature basalt weathering) release large concentrations of Fe^{2+} ions into aquifers, where they are free to oxidize.

4.3. Basalt Hydrothermal Alteration Processes

The DJI-4 study site, which is located between major faults F and D, exhibits hydrothermal alteration that is typical of basalt around fumaroles (96 °C), with the formation of Fe-rich clays. Primary reactions preceded the formation of the clays, forming iddingsite and flame-like bodies of hematite. Iddingsite is a mineralogical assemblage between goethite and clay minerals [107], and its presence suggests that oxidation and hydration of the magma occurred during cooling [108,109]. The reaction is a form of hydrothermal metasomatism and is induced by the interaction of volcanic gases with lava; it results in iron enrichment and magnesium depletion of the mineral assemblage [107]. The formation of characteristic flame-like bodies of hematite associated with forsterite, as observed in olivine near areas of porosity, could be the result of primary oxidation at high temperature (600–1000 °C) [94]. Such reactions don't typically involve water or hydrogen sulfide and so do not result in H_2 generation.

The XRD and Mössbauer data indicate that the system in DJI-4 is highly enriched in Fe^{3+} and depleted in Si and Mg, after alteration with the formation of magnetite and hematite at the expense of olivines and pyroxenes to form Fe-beidellite and Fe-oxides [95]. Ferrihydrite, which is a hydrated Fe^{3+} oxyhydroxide, is an unstable intermediate state and is typically transformed in goethite by dissolution–reprecipitation or in hematite by dehydration–structural rearrangement [110]. Because ferrihydrite is a hydrated phase, we suggest that its formation does not allow, or allows only in small quantities, the production of H_2. However, secondary transformation by dehydration and the assimilation of Fe^{2+} to form hematite and goethite could be a potential generator of hydrogen in the system. The occurrence of these multiple reactions is supported by the clear increase in the Fe^{3+}/Fe^{2+} ratio between the fresh and altered basalt samples.

4.4. H_2 Origins

Only a little bit of hydrogen was present at the surface in our study area. Nevertheless, our data suggest that, in the Fiale area of the Asal Rift, natural hydrogen is generated in the crust by redox reactions between the iron minerals of the basalts and deep fluids at high temperatures (approximately >270 °C); this is supported by isotopic data. We found that hydrogen is concentrated in the fumaroles at the DJI-4 site, between faults F and D.

The surface markers studied at this site indicate that H_2 production from these cooler surface fluids is possible.

As there is no mixing between deep and superficial fluids in the study area, we hypothesize that there are three different sources of natural hydrogen in this setting.

A: A first hydrogen could form at depth, at temperatures of at least 270 °C, in the rift margins in the epidote zone ($H_2{}^a$) via reactions described in previous studies [102,111]. This H_2 would take advantage of the active F and D faults [74] to rise relatively quickly and avoid potential consumption of the H_2 by microorganisms before reaching the surface.

B: A second more proximal hydrogen source at lower temperatures in the smectite zone in the center of the rift ($H_2{}^b$) could form hydrogen according to the following reaction:

$$\text{olivine} + \text{clinopyroxene} + \text{plagioclase} + \text{Ti-magnetite} + \text{ilmenite} + \text{hematite} + H_2O \rightarrow \text{ferrihydrite} + \text{hematite/maghemite} \uparrow + \text{Ti-magnetite} \uparrow + \text{ilmenite} \downarrow + \text{Fe-beidellite} + \text{Mn-oxides} + H_2. \quad (2)$$

C: And finally, the third potential origin of hydrogen in this system is linked to the formation of pyrite ($H_2{}^c$). No iron sulfide was observed in our surface samples. However, pyrite was found in wells, forming mostly at temperatures of 150–350 °C [87]. Therefore, we propose that H_2S could have reacted with pyrrhotite to form pyrite and H_2. Thus, H_2 would be formed not through the oxidation of iron and the reduction in water, but through the oxidation of sulfur and the reduction in H_2S. This mechanism of hydrogen formation has not been studied extensively to date; in particular, it has yet to be fully explored in magmatic settings, as discussed recently by [112].

Sources A and C are supported by the isotopic signatures of the gas mixtures considered here. Indeed, it is interesting to note that both the $\delta^{13}C$ and δ^2H paleothermometers yielded similar equilibrium temperatures (approximately 300 °C). The isotopic signature of CO_2 indicates a mantle source (i.e., $\delta^{13}C$ tending toward −7 per mil). Accordingly, it is possible that the H_2 and CO_2 in this system share the same source, and thus that H_2 is formed through the alteration of magmatic rocks that are deeper than those found in the smectite zone.

4.5. Model of Gas Formation and Circulation in the Asal-Ghoubbet Rift

We have created a schematic diagram to illustrate the structure of the rift and the origins of the different gases in the [74,75,87] (Figure 17).

The main seismic activity in this rift is concentrated between major faults B and F, under the Fiale Caldera, at 2–4 km depth [74,75]. Friction along these faults has also been proposed as a source of H_2 (i.e., mechanoradical production; see [113]). However, in the Fiale case, the continuous nature of the hydrogen flow in the fumaroles contradicts this hypothesis.

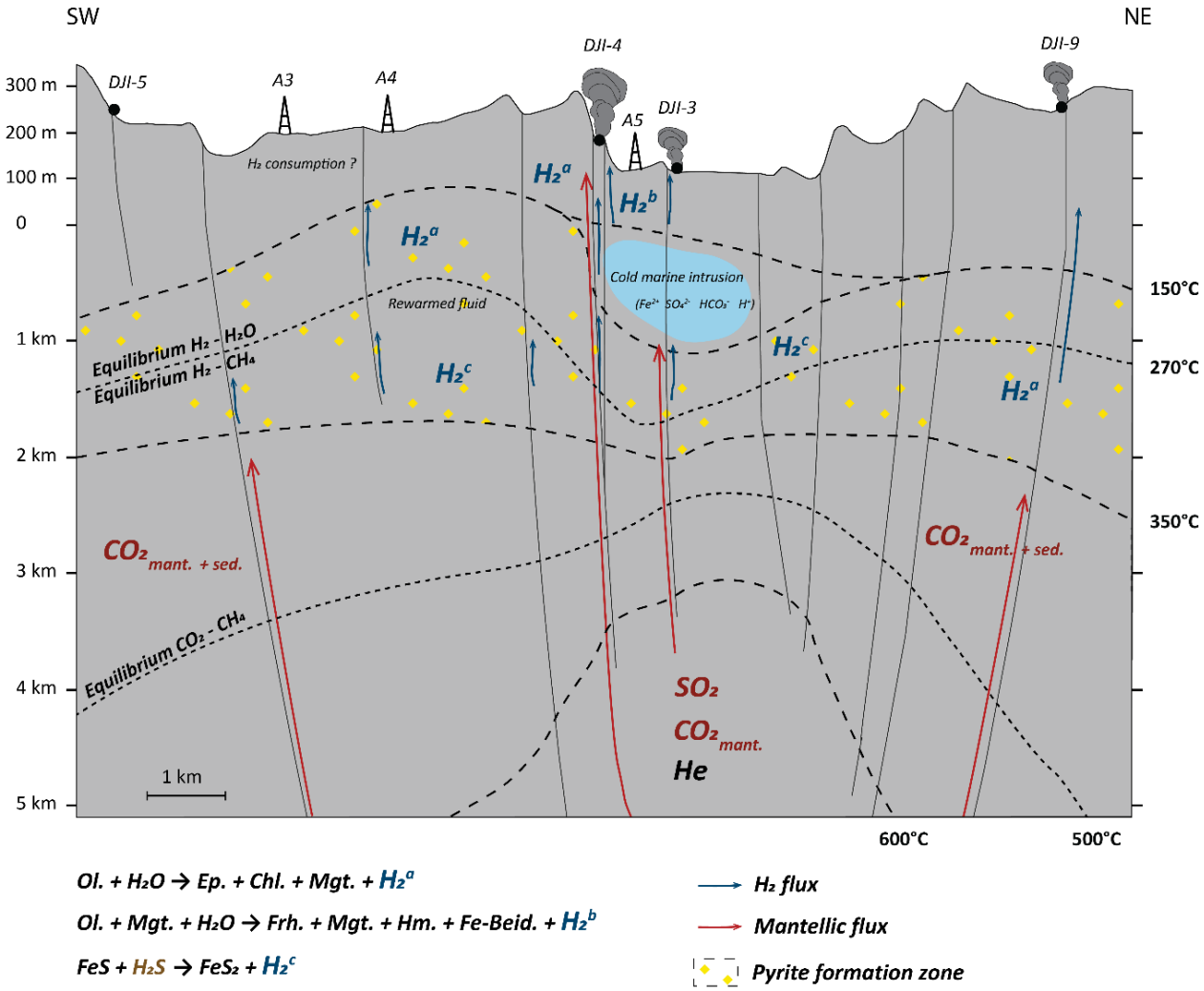

Figure 17. Schematic model of the Asal Rift highlighting gas flows and possible origins of hydrogen measured at the surface in fumaroles. Beid.: beidellite; Chl.: chlorite; Ep.: epidote; Frh.: ferrihydrite; Hm.: hematite; Mgt.: magnetite; Ol.: olivine.

5. Conclusions

This study highlighted potential mechanisms for the generation of H_2 in the central active part of the Asal Rift. We did not find any H_2 surface emanations north of the Asal–Ghoubbet axis, and there were no wells to sample in this area. Similarly, we were unable to sample any wells to the south of the axis, in the other grabens between the Asal Rift and Lake Abhe. Accordingly, our data set is still too limited to make any definitive conclusions regarding the resource potential of H_2 in these zones.

H_2 is generated within the central axis of this active rift system. This production is made possible by water circulation at depth, under high-temperature conditions near a proximal degassing magmatic chamber located along the active rift axis. Despite the various potential origins, there is only a rather scarce H_2 generation in the basalts present, partly owing to their low olivine content; this is similar to some mid-Atlantic vents located on basaltic bedrock. Despite their alkaline character, the basalts of the Asal Rift are similar to those described for oceanic ridges, although the recent basalts of the axial series exhibit iron enrichment [64,114]. Gas contents are spatially variable depending on the proximity of the faults to the magmatic intrusions/magma chamber. Active faults allow magmatic gas ascension, as well as the formation of fumaroles above; gas contents are also enhanced by the shallow marine intrusion under the Fiale Caldera. There is a lack of representative data relating to the Asal Rift over different time periods, making it difficult to compare the Asal

system with the Icelandic system. The hydrogen contents in the Icelandic system exhibit temporal variability, which can be explained in part by magmatic intrusions in aquifers inducing high H_2 concentrations. Except for some cases in Iceland (see above), H_2 contents are typically lower in basalt-hosted hydrothermal fields than in peridotite-hosted fields; this applies to basalt-hosted examples in Iceland [45,102,111,115–117], along the MAR [32], and in Asal [88,91,92].

The low olivine concentrations of the basalts combined with the high salinity of Asal waters (which reduces the solubility of hydrogen in fluids, unlike the Icelandic meteoric/glacial waters) can explain the lower rates of H_2 generation relative to Icelandic examples. The arid climate of the Asal region does not allow sufficient meteoric recharge to induce more abundant oxidoreduction reactions. However, a more continuous measurement record in this region would help constrain gas variations and the involvement of mantle gases. Moreover, additional δD isotope measurements would allow us to test the various hypotheses presented here regarding the origin of hydrogen, particularly if variation in the δD values of the hydrogen contained in the fumaroles was markedly different from that of the hydrogen in the geothermal wells. No or very little gas is visible at the surface outside the rift axis, except as atmospheric contamination, and hydrogen can be consumed on its way to the surface by microorganisms or via reactions with the other gases present.

This study has shown that the Afar region produces natural H_2 and has the mineralogical potential to produce large quantities in the subsurface through fluid–rock interactions. However, deep sampling, and therefore wells, are needed to confirm this assumption. Coupling geothermal exploitation with H_2 exploration could thus present an opportunity for development and joint production. Indeed, H_2 has been described in onshore high-temperature geothermal fields, such as in Iceland and Larderello [45,102,118], and H_2 can be produced in conjunction with geothermal energy, using membrane systems for gas separation, where the flow rate and gas content are sufficiently high.

Author Contributions: This research was mainly conducted by G.P., but is part of a collaboration between UPPA and ODDEG. J.V. shared with us his knowledge of the area and participated in the field acquisition. O.S. and R.H.H. participated in the gas analysis in laboratory and contributed their interpretations. G.P. and I.M.: writing—original draft preparation; J.V. and O.S.: review and editing; I.M.: supervision, project administration, and funding acquisition. All authors have read and agreed to the published version of the manuscript.

Funding: This research was funded by ISIFOR, Carnot.

Data Availability Statement: The data presented in this study are available within the manuscript.

Acknowledgments: The authors are grateful to ISIFoR and E2S UPPA for funding this thesis. We are also grateful to ODDEG for allowing us to collaborate and conduct fieldwork in the Republic of Djibouti. We thank Omar Boudouma from ISTeP and Dan Levy from UPPA for their assistance with the SEM analyses; Patience Ekambas and Helene Vermesse from IFPEN for the gas analysis; Mathieu Duttine from ICMB for the Mössbauer analysis; and Stephen Centrella from UPPA for the microprobe analyses. We would like to thank Lynsey MacLeary, of editing a draft of this manuscript.

Conflicts of Interest: The authors declare no conflict of interest. The funders had no role in the design of the study; in the collection, analyses, or interpretation of data; in the writing of the manuscript, or in the decision to publish the results.

References

1. Moretti, I. H2: Energy Vector or Source? *L'Actualité Chim.* **2019**, *3*, 442.
2. Moretti, I.; Webber, M.E. *Natural Hydrogen: A Geological Curiosity or the Primary Energy Source for a Low-Carbon Future?* 2021; Volume 6, Available online: https://www.renewablematter.eu/articles/article/natural-hydrogen-a-geological-curiosity-or-the-primary-energy-source-for-a-low-carbon-future (accessed on 28 December 2021).
3. Smith, J.; Smith, P.; Wattenbach, M.; Zaehle, S.; Hiederer, R.; Jones, R.J.A.; Montanarella, L.; Rounsevell, M.D.A.; Reginster, I.; Ewert, F. Projected Changes in Mineral Soil Carbon of European Croplands and Grasslands, 1990–2080. *Glob. Chang. Biol.* **2005**, *11*, 2141–2152. [CrossRef]

4. Prinzhofer, A.; Tahara Cissé, C.S.; Diallo, A.B. Discovery of a Large Accumulation of Natural Hydrogen in Bourakebougou (Mali). *Int. J. Hydrogen Energy* **2018**, *43*, 19315–19326. [CrossRef]
5. Gaucher, E.C. New Perspectives in the Industrial Exploration for Native Hydrogen. *Elements* **2020**, *16*, 8–9. [CrossRef]
6. Truche, L.; McCollom, T.M.; Martinez, I. Hydrogen and Abiotic Hydrocarbons: Molecules That Change the World. *Elements* **2020**, *16*, 13–18. [CrossRef]
7. Deville, E.; Prinzhofer, A. The Origin of N2-H2-CH4-Rich Natural Gas Seepages in Ophiolitic Context: A Major and Noble Gases Study of Fluid Seepages in New Caledonia. *Chem. Geol.* **2016**, *440*, 139–147. [CrossRef]
8. Vacquand, C.; Deville, E.; Beaumont, V.; Guyot, F.; Sissmann, O.; Pillot, D.; Arcilla, C.; Prinzhofer, A. Reduced Gas Seepages in Ophiolitic Complexes: Evidences for Multiple Origins of the H2-CH4-N2 Gas Mixtures. *Geochim. Cosmochim. Acta* **2018**, *223*, 437–461. [CrossRef]
9. Larin, N.; Zgonnik, V.; Rodina, S.; Deville, E.; Prinzhofer, A.; Larin, V.N. Natural Molecular Hydrogen Seepage Associated with Surficial, Rounded Depressions on the European Craton in Russia. *Nat. Resour. Res.* **2015**, *24*, 369–383. [CrossRef]
10. Zgonnik, V.; Beaumont, V.; Deville, E.; Larin, N.; Pillot, D.; Farrell, K.M. Evidence for Natural Molecular Hydrogen Seepage Associated with Carolina Bays (Surficial, Ovoid Depressions on the Atlantic Coastal Plain, Province of the USA). *Prog. Earth Planet. Sci.* **2015**, *2*, 31. [CrossRef]
11. Moretti, I.; Prinzhofer, A.; Françolin, J.; Pacheco, C.; Rosanne, M.; Rupin, F.; Mertens, J. Long-Term Monitoring of Natural Hydrogen Superficial Emissions in a Brazilian Cratonic Environment. Sporadic Large Pulses versus Daily Periodic Emissions. *Int. J. Hydrogen Energy* **2021**, *46*, 3615–3628. [CrossRef]
12. Prinzhofer, A.; Moretti, I.; Françolin, J.; Pacheco, C.; D'Agostino, A.; Werly, J.; Rupin, F. Natural Hydrogen Continuous Emission from Sedimentary Basins: The Example of a Brazilian H2-Emitting Structure. *Int. J. Hydrogen Energy* **2019**, *44*, 5676–5685. [CrossRef]
13. Boreham, C.J.; Sohn, J.H.; Cox, N.; Williams, J.; Hong, Z.; Kendrick, M.A. Hydrogen and Hydrocarbons Associated with the Neoarchean Frog's Leg Gold Camp, Yilgarn Craton, Western Australia. *Chem. Geol.* **2021**, *575*, 120098. [CrossRef]
14. Moretti, I.; Brouilly, E.; Loiseau, K.; Prinzhofer, A.; Deville, E. Hydrogen Emanations in Intracratonic Areas: New Guide Lines for Early Exploration Basin Screening. *Geosciences* **2021**, *11*, 145. [CrossRef]
15. Charlou, J.L.; Donval, J.P.; Fouquet, Y.; Jean-Baptiste, P.; Holm, N. Geochemistry of High H2 and CH4 Vent Fluids Issuing from Ultramafic Rocks at the Rainbow Hydrothermal Field (36j14VN, MAR). *Chem. Geol.* **2002**, *191*, 345–359. [CrossRef]
16. Charlou, J.L.; Fouquet, Y.; Bougault, H.; Donval, J.P.; Etoubleau, J.; Jean-Baptiste, P.; Dapoigny, A.; Appriou, P.; Rona, P.A. Intense CH4 Plumes Generated by Serpentinization of Ultramafic Rocks at the Intersection of the 15°20′ N Fracture Zone and the Mid-Atlantic Ridge. *Geochim. Cosmochim. Acta* **1998**, *62*, 2323–2333. [CrossRef]
17. Kelley, D.S. A Serpentinite-Hosted Ecosystem: The Lost City Hydrothermal Field. *Science* **2005**, *307*, 1428–1434. [CrossRef] [PubMed]
18. Kelley, D.S.; Karson, J.A.; Blackman, D.K.; Olson, E.J.; Schrenk, M.O.; Roe, K.K. An Off-Axis Hydrothermal Vent ®eld near the Mid-Atlantic Ridge at 30°N. *Nature* **2001**, *412*, 145–149. [CrossRef] [PubMed]
19. Kelley, D.S.; Baross, J.A.; Delaney, J.R. Volcanoes, Fluids, and Life at Mid-Ocean Ridge Spreading Centers. *Annu. Rev. Earth Planet. Sci.* **2002**, *30*, 385–491. [CrossRef]
20. Baross, J.A.; Hoffman, S.E. Submarine Hydrothermal Vents and Associated Gradient Environments as Sites for the Origin and Evolution of Life. *Orig. Life Evol. Biosph.* **1985**, *15*, 327–345. [CrossRef]
21. Edmond, J.M.; Campbell, A.C.; Palmer, M.R.; Klinkhammer, G.P.; German, C.R.; Edmonds, H.N.; Elderfield, H.; Thompson, G.; Rona, P. Time Series Studies of Vent Fluids from the TAG and MARK Sites (1986, 1990) Mid-Atlantic Ridge: A New Solution Chemistry Model and a Mechanism for Cu/Zn Zonation in Massive Sulphide Orebodies. *Geol. Soc. Lond. Spec. Publ.* **1995**, *87*, 77–86. [CrossRef]
22. Tivey, M.K.; Humphris, S.E.; Thompson, G.; Hannington, M.D.; Rona, P.A. Deducing Patterns of Fluid Flow and Mixing within the TAG Active Hydrothermal Mound Using Mineralogical and Geochemical Data. *J. Geophys. Res.* **1995**, *100*, 12527–12555. [CrossRef]
23. Von Damm, K.L.; Lilley, M.D.; Iii, W.C.S.; Brockington, M.; Bray, A.M.; O'Grady, K.M.; Olson, E.; Graham, A.; Proskurowski, G. Extraordinary Phase Separation and Segregation in Vent Fluids from the Southern East Pacific Rise. *Earth Planet. Sci. Lett.* **2003**, *206*, 365–378. [CrossRef]
24. Douville, E.; Charlou, J.L.; Oelkers, E.H.; Bienvenu, P.; Colon, C.F.J.; Donval, J.P.; Fouquet, Y.; Prieur, D.; Appriou, P. The Rainbow Vent Fluids (36°14′N, MAR): The Influence of Ultramafic Rocks and Phase Separation on Trace Metal Content in Mid-Atlantic Ridge Hydrothermal f Luids. *Chem. Geol.* **2002**, *12*. [CrossRef]
25. Früh-Green, G.L. 30,000 Years of Hydrothermal Activity at the Lost City Vent Field. *Science* **2003**, *301*, 495–498. [CrossRef]
26. Mével, C. Serpentinization of abyssal peridotites at mid-ocean ridges. *Comptes Rendus Geosci.* **2003**, *335*, 825–852. [CrossRef]
27. Kelemen, P.B.; Matter, J. In Situ Carbonation of Peridotite for CO_2 Storage. *Proc. Natl. Acad. Sci. USA* **2008**, *105*, 17295–17300. [CrossRef]
28. Andreani, M.; Mével, C.; Boullier, A.-M.; Escartín, J. Dynamic Control on Serpentine Crystallization in Veins: Constraints on Hydration Processes in Oceanic Peridotites: Serpentine Crystallization. *Geochem. Geophys. Geosyst.* **2007**, *8*, n/a. [CrossRef]

29. Blackman, D.K.; Karson, J.A.; Kelley, D.S.; Cann, J.R.; Früh-Green, G.L.; Gee, J.S.; Hurst, S.D.; John, B.E.; Morgan, J.; Nooner, S.L.; et al. Geology of the Atlantis Massif (Mid-Atlantic Ridge, 30° N): Implications for the Evolution of an Ultramafic Oceanic Core Complex. *Mar. Geophys. Res.* **2002**, *23*, 443–469. [CrossRef]
30. Cannat, M.; Rommevaux-Jestin, C.; Fujimoto, H. Melt Supply Variations to a Magma-Poor Ultra-Slow Spreading Ridge (Southwest Indian Ridge 61° to 69°E): Melt Supply Variations. *Geochem. Geophys. Geosyst.* **2003**, *4*. [CrossRef]
31. Combaudon, V. Evolution des gaz associes à l'ouverture des rides océaniques: Cas de l'hydrogène naturel en Islande. **2020**, *42*.
32. Charlou, J.L.; Donval, J.P.; Konn, C.; Ondréas, H.; Fouquet, Y.; Jean-Baptiste, P.; Fourré, E. High Production and Fluxes of H2 and CH4 and Evidence of Abiotic Hydrocarbon Synthesis by Serpentinization in Ultramafic-Hosted Hydrothermal Systems on the Mid-Atlantic Ridge. In *Diversity of Hydrothermal Systems on Slow Spreading Ocean Ridges*; Geophysical Monograph Series; Rona, P.A., Devey, C.W., Dyment, J., Murton, B.J., Eds.; American Geophysical Union: Washington, DC, USA, 2010; Volume 188, pp. 265–296. ISBN 978-0-87590-478-8.
33. Kularatne, K.; Sissmann, O.; Kohler, E.; Chardin, M.; Noirez, S.; Martinez, I. Simultaneous Ex-Situ CO_2 Mineral Sequestration and Hydrogen Production from Olivine-Bearing Mine Tailings. *Appl. Geochem.* **2018**, *95*, 195–205. [CrossRef]
34. Sissmann, O.; Brunet, F.; Martinez, I.; Guyot, F.; Verlaguet, A.; Pinquier, Y.; Daval, D. Enhanced Olivine Carbonation within a Basalt as Compared to Single-Phase Experiments: Reevaluating the Potential of CO_2 Mineral Sequestration. *Environ. Sci. Technol.* **2014**, *48*, 5512–5519. [CrossRef] [PubMed]
35. Stevens, T.O.; McKinley, J.P. Abiotic Controls on H_2 Production from Basalt−Water Reactions and Implications for Aquifer Biogeochemistry. *Environ. Sci. Technol.* **2000**, *34*, 826–831. [CrossRef]
36. McCollom, T.M.; Bach, W. Thermodynamic Constraints on Hydrogen Generation during Serpentinization of Ultramafic Rocks. *Geochim. Cosmochim. Acta* **2009**, *73*, 856–875. [CrossRef]
37. Seyfried, W.E.; Foustoukos, D.I.; Fu, Q. Redox Evolution and Mass Transfer during Serpentinization: An Experimental and Theoretical Study at 200 °C, 500bar with Implications for Ultramafic-Hosted Hydrothermal Systems at Mid-Ocean Ridges. *Geochim. Cosmochim. Acta* **2007**, *71*, 3872–3886. [CrossRef]
38. Honnorez, J.J.; Alt, J.C.; Humphris, S.E. (Eds.) Vivisection and Autopsy of Active and Fossil Hydrothermal Alterations of Basalt beneath and within the TAG Hydrothermal Mound. In Proceedings of the Ocean Drilling Program; IODP Publication Services, Texas A&M University: College Station, TX, USA, 1998; Volume 158.
39. Seewald, J.S.; Seyfried, W.E. The Effect of Temperature on Metal Mobility in Subseafloor Hydrothermal Systems: Constraints from Basalt Alteration Experiments. *Earth Planet. Sci. Lett.* **1990**, *101*, 388–403. [CrossRef]
40. Seyfried, W.; Bischoff, J.L. Hydrothermal Transport of Heavy Metals by Seawater: The Role of Seawater/Basalt Ratio. *Earth Planet. Sci. Lett.* **1977**, *34*, 71–77. [CrossRef]
41. Reed, M.H.; Palandri, J. Hydrogen Produced by Reduction of H2O in Rock Reaction: Peridotite vs. Basalt. In *AIP Conference Proceedings*; AIP: Sendai, Japan, 2008; Volume 987, pp. 100–104.
42. Ménez, B. Abiotic Hydrogen and Methane: Fuels for Life. *Elements* **2020**, *16*, 39–46. [CrossRef]
43. Prieur, D.; Erauso, G.; Jeanthon, C. Hyperthermophilic Life at Deep-Sea Hydrothermal Vents. *Planet. Space Sci.* **1995**, *43*, 115–122. [CrossRef]
44. Nonn, C.; Leroy, S.; Khanbari, K.; Ahmed, A. Tectono-Sedimentary Evolution of the Eastern Gulf of Aden Conjugate Passive Margins: Narrowness and Asymmetry in Oblique Rifting Context. *Tectonophysics* **2017**, *721*, 322–348. [CrossRef]
45. Arnórsson, S.; Gunnlaugsson, E. New Gas Geothermometers for Geothermal Exploration—Calibration and Application. *Geochim. Cosmochim. Acta* **1985**, *49*, 1307–1325. [CrossRef]
46. Stefánsson, A. Gas Chemistry of Icelandic Thermal Fluids. *J. Volcanol. Geotherm. Res.* **2017**, *346*, 81–94. [CrossRef]
47. Arnórsson, S. Gas Pressures in Geothermal Systems. *Chem. Geol.* **1985**, *49*, 319–328. [CrossRef]
48. D'Amore, F.; Panichi, C. Evaluation of Deep Temperatures of Hydrothermal Systems by a New Gas Geothermometer. *Geochim. Cosmochim. Acta* **1980**, *44*, 549–556. [CrossRef]
49. D'Amore, F.; Truesdell, A.H. Calculation of Geothermal Reservoir Temperatures and Steam Fractions from Gas Compositions. *Trans. Geotherm.* **1985**, *9*, 305–310.
50. Giggenbach, W.F. Geothermal Gas Equilibria. *Geochim. Cosmochim. Acta* **1980**, *44*, 2021–2032. [CrossRef]
51. Barberi, F.; Ferrara, G.; Santacroce, R.; Treuil, M.; Varet, J. A Transitional Basalt-Pantellerite Sequence of Fractional Crystallization, the Boina Centre (Afar Rift, Ethiopia). *J. Petrol.* **1975**, *16*, 22–56. [CrossRef]
52. Tazieff, H.; Varet, J.; Barberi, F.; Giglia, G. Tectonic Significance of the Afar (or Danakil) Depression. *Nature* **1972**, *235*, 144–147. [CrossRef]
53. Craig, T.J.; Jackson, J.A.; Priestley, K.; McKenzie, D. Earthquake Distribution Patterns in Africa: Their Relationship to Variations in Lithospheric and Geological Structure, and Their Rheological Implications: Earthquake Distribution Patterns in Africa. *Geophys. J. Int.* **2011**, *185*, 403–434. [CrossRef]
54. Chorowicz, J. The East African Rift System. *J. Afr. Earth Sci.* **2005**, *43*, 379–410. [CrossRef]
55. Chorowicz, J.; Fournier, J.L.; Vidal, G. A Model for Rift Development in Eastern Africa. *Geol. J.* **1987**, *22*, 495–513. [CrossRef]
56. Bosworth, W.; Huchon, P.; McClay, K. The Red Sea and Gulf of Aden Basins. *J. Afr. Earth Sci.* **2005**, *43*, 334–378. [CrossRef]
57. Purcell, P.G. Re-Imagining and Re-Imaging the Development of the East African Rift. *Pet. Geosci.* **2018**, *24*, 21–40. [CrossRef]
58. Mohr, P. Ethiopian Flood Basalt Province. *Nature* **1983**, *303*, 577–584. [CrossRef]

59. Nonn, C.; Leroy, S.; Lescanne, M.; Castilla, R. Central Gulf of Aden Conjugate Margins (Yemen-Somalia): Tectono-Sedimentary and Magmatism Evolution in Hybrid-Type Margins. *Mar. Pet. Geol.* **2019**, *105*, 100–123. [CrossRef]
60. Moretti, I.; Colletta, B. Spatial and Temporal Evolution of the Suez Rift Subsidence. *J. Geodyn.* **1987**, *7*, 151–168. [CrossRef]
61. Barberi, F.; Borsi, S.; Ferrara, G.; Marinelli, G.; Santacroce, R.; Tazieff, H.; Varet, J. Evolution of the Danakil Depression (Afar, Ethiopia) in Light of Radiometric Age Determinations. *J. Geol.* **1972**, *80*, 720–729. [CrossRef]
62. Barberi, F.; Varet, J. Volcanism of Afar: Small-Scale Plate Tectonics Implications. *GSA Bull.* **1977**, *88*, 1251–1266. [CrossRef]
63. Barberi, F.; Varet, J. The Erta Ale Volcanic Range (Danakil Depression, Northern Afar, Ethiopia). *Bull. Volcanol.* **1970**, *34*, 848–917. [CrossRef]
64. Stieltjes, L.; Joron, J.L.; Treuil, M.; Varet, J. Le rift d'Asal, segment de dorsale emerge; discussion petrologique et geochimique. *Bull. Société Géologique Fr.* **1976**, *S7-XVIII*, 851–862. [CrossRef]
65. Stab, M.; Bellahsen, N.; Pik, R.; Quidelleur, X.; Ayalew, D.; Leroy, S. Modes of Rifting in Magma-Rich Settings: Tectono-Magmatic Evolution of Central Afar: Modes of Rifting in Magma-Rich Settings. *Tectonics* **2016**, *35*, 2–38. [CrossRef]
66. Varet, J. *Carte Géologique de l'Afar Central et Méridional (Éthiopie et T.F.A.I.) =: Geological Map of Central and Southern Afar (Ethiopia and F.T.A.I.)*; CNRS: Paris, France, 1978.
67. Doubre, C.; Déprez, A.; Masson, F.; Socquet, A.; Lewi, E.; Grandin, R.; Nercessian, A.; Ulrich, P.; De Chabalier, J.-B.; Saad, I.; et al. Current Deformation in Central Afar and Triple Junction Kinematics Deduced from GPS and InSAR Measurements. *Geophys. J. Int.* **2017**, *208*, 936–953. [CrossRef]
68. Saria, E.; Calais, E.; Altamimi, Z.; Willis, P.; Farah, H. A New Velocity Field for Africa from Combined GPS and DORIS Space Geodetic Solutions: Contribution to the Definition of the African Reference Frame (AFREF): An African Geodetic Reference Frame. *J. Geophys. Res. Solid Earth* **2013**, *118*, 1677–1697. [CrossRef]
69. Stamps, D.S.; Calais, E.; Saria, E.; Hartnady, C.; Nocquet, J.-M.; Ebinger, C.J.; Fernandes, R.M. A Kinematic Model for the East African Rift. *Geophys. Res. Lett.* **2008**, *35*, L05304. [CrossRef]
70. Agostini, A.; Bonini, M.; Corti, G.; Sani, F.; Mazzarini, F. Fault Architecture in the Main Ethiopian Rift and Comparison with Experimental Models: Implications for Rift Evolution and Nubia–Somalia Kinematics. *Earth Planet. Sci. Lett.* **2011**, *301*, 479–492. [CrossRef]
71. Mohr, P.A. The Afar Triple Junction and Sea-Floor Spreading. *J. Geophys. Res.* **1970**, *75*, 7340–7352. [CrossRef]
72. Le Dain, A.Y.; Robineau, B.; Tapponier, P. Les Effets Tectoniques de l'évenement Sismique et Volcanique de Novembre 1978 Dans Le Rift d'Asal-Ghoubbet. *Palaeogeogr. Palaeoclimatol. Palaeoecol.* **1978**, *24*, 279–325. [CrossRef]
73. Tapponier, P.; Varet, J. La Zone de Mak'arrasou En Afar: Un Équivalent Émergé Des "Failles Transformantes" Océaniques. *Comptes Rendus Acad. Sci.* **1974**, *278*, 317–329.
74. Doubre, C.; Manighetti, I.; Dorbath, C.; Dorbath, L.; Jacques, E.; Delmond, J.C. Crustal Structure and Magmato-Tectonic Processes in an Active Rift (Asal-Ghoubbet, Afar, East Africa): 1. Insights from a 5-Month Seismological Experiment. *J. Geophys. Res.* **2007**, *112*, B05405. [CrossRef]
75. Doubre, C.; Peltzer, G. Fluid-Controlled Faulting Process in the Asal Rift, Djibouti, from 8 Yr of Radar Interferometry Observations. *Geology* **2007**, *35*, 69. [CrossRef]
76. Varet, J. Asal-Fialé Geothermal Field (Djibouti Republic): A New Interpretation for a Geothermal Reservoir in an Actively Spreading Rift Segment. In Proceedings of the 5th African Rift geothermal Conference, Arusha, Tanzania, 29–31 October 2014; p. 9.
77. Bosch, B.; Deschamps, J.; Leleu, M.; Lopoukhine, M.; Marce, A.; Vilbert, C. The Geothermal Zone of Lake Assal (F.T.A.I.), Geochemical and Experimental Studies. *Geothermics* **1977**, *5*, 165–175. [CrossRef]
78. Fouillac, A.M.; Fouillac, C.; Cesbron, F.; Pillard, F.; Legendre, O. Water-Rock Interaction between Basalt and High-Salinity Fluids in the Asal Rift, Republic of Djibouti. *Chem. Geol.* **1989**, *76*, 271–289. [CrossRef]
79. Mlynarski, M.; Zlotnicki, J. Fluid Circulation in the Active Emerged Asal Rift (East Africa, Djibouti) Inferred from Self-Potential and Telluric–Telluric Prospecting. *Tectonophysics* **2001**, *339*, 455–472. [CrossRef]
80. Sanjuan, B.; Michard, G.; Michard, A. Origine des substances dissoutes dans les eaux des sources thermales et des forages de la région Asal-Ghoubbet (République de Djibouti). *J. Volcanol. Geotherm. Res.* **1990**, *43*, 333–352. [CrossRef]
81. Delibrias, G.; Marinelli, G.; Stieltjes, L. *Spreading Rate of the Asal Rift: A Geological Approach*; Schweizerbart: Stuttgart, Germany, 1975; Volume 1, ISBN 3-510-65069-7.
82. Vigny, C.; de Chabalier, J.-B.; Ruegg, J.-C.; Huchon, P.; Feigl, K.L.; Cattin, R.; Asfaw, L.; Kanbari, K. Twenty-Five Years of Geodetic Measurements along the Tadjoura-Asal Rift System, Djibouti, East Africa. *J. Geophys. Res.* **2007**, *112*, B06410. [CrossRef]
83. Fournier, M.; Gasse, F.; Lépine, J.-C.; ORSTOM (France). Institut Supérieur d'études et de Recherches Scientifiques et Techniques (Djibouti) Carte Géologique de la République de Djibouti. [NC-38-XIX-4], [NC-38-XIX-4], 1984. Available online: https://www.sudoc.fr/124662544 (accessed on 28 December 2021).
84. Boudouma, O. Etude Pétrologique Des Laves Basaltiques Du Rift d'Asal (DJIBOUTI). Ph.D. Thesis, Université Pierre et Marie Curie (Paris VI), Paris, France, 1997.
85. Demange, J.; Stieltjes, L.; Varet, J. L'Eruption d'Asal de novembre 1978. *Bull. Société Géologique Fr.* **1980**, *S7-XXII*, 837–843. [CrossRef]
86. Houssein, D.E.; Axelsson, G. Geothermal Resources in the Asal Region, Republic of Djibouti: An Update with Emphasis on Reservoir Engineering Studies. *Geothermics* **2010**, *39*, 220–227. [CrossRef]

87. Zan, L.; Gianelli, G.; Troisi, C.; Haga, A.O. Geothermal exploration in the republic of djibouti: Thermal and geological data of the hanlt and asal areas. *Geothermics* **1990**, *19*, 561–582. [CrossRef]
88. D'Amore, F.; Giusti, D.; Abdallah, A. Geochemistry of the High-Salinity Geothermal Field of Asal, Republic of Djibouti, Africa. *Geothermics* **1998**, *27*, 197–210. [CrossRef]
89. Bottinga, Y. Calculated Fractionation Factors for Carbon and Hydrogen Isotope Exchange in the System Calcite-Carbon Dioxide-Graphite-Methane-Hydrogen-Water Vapor. *Geochim. Cosmochim. Acta* **1969**, *33*, 49–64. [CrossRef]
90. Horibe, Y.; Craig, H. Fractionation in the System Methane-Hydrogen-Water. *Geochim. Cosmochim. Acta* **1995**, *59*, 5209–5217. [CrossRef]
91. Darling, W.G. *The Geochemistry of Fluid Processes in the Eastern Branch of the East African Rift System*; Open University: Milton Keynes, UK, 1996. [CrossRef]
92. Allard, P.; Tazieff, H.; Dajlevic, D. Observations of Seafloor Spreading in Afar during the November 1978 Fissure Eruption. *Nature* **1979**, *279*, 30–33. [CrossRef]
93. Dekov, V.M.; Egueh, N.M.; Kamenov, G.D.; Bayon, G.; Lalonde, S.V.; Schmidt, M.; Liebetrau, V.; Munnik, F.; Fouquet, Y.; Tanimizu, M.; et al. Hydrothermal Carbonate Chimneys from a Continental Rift (Afar Rift): Mineralogy, Geochemistry, and Mode of Formation. *Chem. Geol.* **2014**, *387*, 87–100. [CrossRef]
94. Haggerty, S.E.; Baker, I. The Alteration of Olivine in Basaltic and Associated Lavas. *Contrib. Mineral. Petrol.* **1967**, *16*, 233–257. [CrossRef]
95. Meunier, A. *Clays*; Springer: Berlin/Heidelberg, Germany; New York, NY, USA, 2005; ISBN 978-3-540-21667-4.
96. Miglierini, M.; Petridis, D. (Eds.) *Mössbauer Spectroscopy in Materials Science*; Springer: Dordrecht, The Netherlands, 1999; ISBN 978-0-7923-5641-7.
97. Stevens, J.G.; Khasanov, A.M.; Miller, J.W.; Pollak, H.; Li, Z. *Mössbauer Mineral Handbook*; Medc: Dalian, China, 2005; p. 636.
98. Sassi, M.; Rosso, K.M. Roles of Hydration and Magnetism on the Structure of Ferrihydrite from First Principles. *ACS Earth Space Chem.* **2019**, *3*, 70–78. [CrossRef]
99. Alt, J.C.; Honnorez, J. Alteration of the Upper Oceanic Crust, DSDP Site 417: Mineralogy and Chemistry. *Contrib. Mineral. Petrol.* **1984**, *87*, 149–169. [CrossRef]
100. Deer, W.A.; Howie, R.A.; Zussman, J. *An Introduction to the Rock-Forming Minerals*, 3rd ed.; The Minerological Society: London, UK, 2013; ISBN 978-0-903056-33-5.
101. Haas, J.L. The Effect of Salinity on the Maximum Thermal Gradient of a Hydrothermal System at Hydrostatic Pressure. *Econ. Geol.* **1971**, *66*, 940–946. [CrossRef]
102. Oskarsson, N. Monitoring of Fumarole Discharge during the 1975–1982 Rifting in Krafla Volcanic Center, North Iceland. *J. Volcanol. Geotherm. Res.* **1984**, *22*, 97–121. [CrossRef]
103. Correia, H.; Fouillac, C.; Gerard, A.; Varet, J. The Asal Geothermal Field (Republic of Djibouti). 1985, Volume 8, pp. 513–519. Available online: publications.mygeoenergynow.org/grc/1001487.pdf (accessed on 28 December 2021).
104. Etiope, G. Abiotic Methane in Continental Serpentinization Sites: An Overview. *Procedia Earth Planet. Sci.* **2017**, *17*, 9–12. [CrossRef]
105. Etiope, G.; Sherwood Lollar, B. Abiotic methane on earth: Abiotic methane on earth. *Rev. Geophys.* **2013**, *51*, 276–299. [CrossRef]
106. Helgeson, H.C. Thermodynamics of Hydrothermal Systems at Elevated Temperatures and Pressures. *Am. J. Sci.* **1969**, *267*, 729–804. [CrossRef]
107. Lemaitre, O.; Brousse, R.; Goñi, J.C.; Remond, G. Sur l'importance de l'apport de fer dans la transformation de l'olivine en iddingsite. *Bulmi* **1966**, *89*, 477–483. [CrossRef]
108. Edwards, A.B. The formation of iddingsite. *Am. Mineral.: J. Earth Planet. Mater.* **1938**, *23*, 277–281.
109. Ross, C.S.; Shannon, E.V. The Origin, Occurrence, Composition, and Physical Properties of the Mineral Iddingsite. *Proc. U. S. Natl. Mus.* **1925**, *67*, 1–19. [CrossRef]
110. Wang, X.; Zhu, M.; Lan, S.; Ginder-Vogel, M.; Liu, F.; Feng, X. Formation and Secondary Mineralization of Ferrihydrite in the Presence of Silicate and Mn(II). *Chem. Geol.* **2015**, *415*, 37–46. [CrossRef]
111. Ármannsson, H.; Gíslason, G.; Hauksson, T. Magmatic Gases in Well Fluids Aid the Mapping of the Flow Pattern in a Geothermal System. *Geochim. Cosmochim. Acta* **1982**, *46*, 167–177. [CrossRef]
112. Arrouvel, C.; Prinzhofer, A. Genesis of Natural Hydrogen: New Insights from Thermodynamic Simulations. *Int. J. Hydrogen Energy* **2021**, *46*, 18780–18794. [CrossRef]
113. Klein, F.; Tarnas, J.D.; Bach, W. Abiotic Sources of Molecular Hydrogen on Earth. *Elements* **2020**, *16*, 19–24. [CrossRef]
114. Bass, M.N. Variable Abyssal Basalt Populations and Their Relation to Sea-Floor Spreading Rates. *Earth Planet. Sci. Lett.* **1971**, *11*, 18–22. [CrossRef]
115. Ármannsson, H.; Benjamínsson, J.; Jeffrey, A.W.A. Gas Changes in the Krafla Geothermal System, Iceland. *Chem. Geol.* **1989**, *76*, 175–196. [CrossRef]
116. Sano, Y.; Urabe, A.; Wakita, H.; Chiba, H.; Sakai, H. Chemical and Isotopic Compositions of Gases in Geothermal Fluids in Iceland. *Geochem. J.* **1985**, *19*, 14. [CrossRef]

117. Scott, S.; Gunnarsson, I.; Arnórsson, S.; Stefánsson, A. Gas Chemistry, Boiling and Phase Segregation in a Geothermal System, Hellisheidi, Iceland. *Geochim. Cosmochim. Acta* **2014**, *124*, 170–189. [CrossRef]
118. Leila, M.; Levy, D.; Battani, A.; Piccardi, L.; Segvic, B.; Badurina, L.; Pasquet, G.; Combaudon, V.; Moretti, I. Origin of Continuous Hydrogen Flux in Gas Manifestations at the Larderello Geothermal Field, Central Italy. *Chem. Geol.* **2021**, *585*, 120564. [CrossRef]